Optical parametric amplifiers using chirped quasi-phase-matching gratings I: practical design formulas

Mathieu Charbonneau-Lefort,[1,*] Bedros Afeyan,[2] and M. M. Fejer[2]

[1]*E. L. Ginzton Laboratory, Stanford University, Stanford, California 94305, USA*
[2]*Polymath Research Inc., Pleasanton, California 94566, USA*
[*]*Corresponding author: mathieu@polymath-usa.com*

Received August 20, 2007; revised January 15, 2008; accepted January 17, 2008;
posted January 24, 2008 (Doc. ID 86421); published March 6, 2008

Optical parametric amplifiers using chirped quasi-phase-matching (QPM) gratings offer the possibility of engineering the gain and group delay spectra. We give practical formulas for the design of such amplifiers. We consider linearly chirped QPM gratings providing constant gain over a broad bandwidth, sinusoidally modulated profiles for selective frequency amplification and a pair of QPM gratings working in tandem to ensure constant gain and constant group delay at the same time across the spectrum. The analysis is carried out in the frequency domain using Wentzel–Kramers–Brillouin analysis. © 2008 Optical Society of America

OCIS codes: 140.4480, 190.4970, 190.4410, 190.7110, 320.1590, 320.5540.

1. INTRODUCTION

Several scientific and technological applications require short optical pulses with large peak power [1]. A number of practical mode-locked femtosecond oscillators are available, but scaling from nanojoule pulse energies to millijoules and above generally requires optical amplification [2]. The chirped-pulse amplification technique [3], which avoids the undesired effects associated with large peak power by first stretching the optical pulse and then recompressing it after the amplification stage, made amplification possible over 9 orders of magnitude while enabling high-pulse energies.

Solid-state optical amplifiers have played a major role in the development of high-power laser systems [1,2]. However a limitation of solid-state laser amplifiers lies in the fact that their gain spectrum is determined by a particular atomic transition. This determines the operating wavelength and limits the amplification bandwidth.

Optical parametric amplifiers (OPAs) provide a solution to this problem. OPAs allow a wider choice of pump and signal wavelengths. Their large single-pass gain avoids the need for complex multipass or regenerative configurations. Moreover, parametric amplifiers do not rely on optical absorption as a pumping mechanism, thus eliminating the problem of thermal lensing common to high average-power systems. Their use as femtosecond pulse amplifiers [4–6] and their use in chirped-pulse amplification systems [7] has been successfully demonstrated.

There are two techniques commonly used to broaden the amplification bandwidth of OPAs. The first one is to operate at degeneracy, where the signal and idler wavelengths are equal. In this case the group velocities of the waves are matched, which leads to a broad amplification bandwidth. Chirped-pulse amplification systems using this technique are described in [8–10]. A drawback of operating at degeneracy is that the wavelength required from the pump laser is fixed once the center of the gain spectrum is chosen, precluding the use of convenient pump lasers in some applications. Another disadvantage is that the bandwidth, although larger than in a nondegenerate case, remains limited by the dispersion of the material.

The second bandwidth-broadening technique involves a noncollinear geometry [11]. The input signal beam is dispersed angularly using diffraction gratings in order to ensure simultaneously phase matching and group-velocity matching between the signal and idler waves. Amplification of pulses as short as 5 fs was achieved using this method [12,13].

A less complicated approach, collinear in nature, is to use chirped quasi-phase-matching (QPM) gratings in order to build broadband OPAs. This is the technique explored in this paper.

The QPM technique consists of a periodic reversal of the sign of the nonlinear coefficient in order to compensate for the accumulated phase mismatch [14]. Since the period of the sign reversal is a controlled parameter, QPM devices operate equally well over a range of wavelengths. QPM allows more freedom over the choice of polarization of the waves than birefringent phase matching, enabling the use of the largest component of the nonlinear susceptibility tensor. For these reasons, QPM gratings have become a widely used alternative to traditional birefringent phase matching. In particular, femtosecond-pulse amplifiers based on QPM materials have been successfully demonstrated [15–17].

In addition to the benefits mentioned above, QPM offers a distinct advantage over conventional nonlinear crystals. It allows the engineering of nonuniform phase-matching profiles, which can be used to obtain desirable and highly tunable gain and phase spectra. For instance,

chirped QPM gratings have been used to broaden the second-harmonic acceptance bandwidth [18] and to manipulate the phase of the generated wave in order to achieve pulse compression [19–23]. Previous work in the context of OPA includes the calculation of the single-pass gain [24], the use of aperiodic QPM gratings in optical parametric oscillators [25], and the proposal of a tandem-grating design for the simultaneous control of the gain and group delay [26].

This paper is an investigation of the properties of chirped QPM gratings used as broadband OPAs. The easiest model to describe OPAs is the Rosenbluth model [27], which is presented in Section 2. In Section 3, we give expressions for the amplitude and phase response of any slow-varying QPM grating profile and explore a variety of designs in Section 4. We look at the linear phase-matching profile in depth. It is the most important in practice because it allows one to achieve an essentially constant gain over a wide bandwidth. We also consider apodization techniques to reduce the gain and phase ripple. We then explore the effect of a sinusoidal modulation of the grating profile, which provides selective amplification at certain frequencies. Finally, we describe a tandem-grating design that achieves constant gain and constant group delay across the spectrum. We also give a short discussion of parametric amplification in the low-gain regime, showing the connection with the work done in the context of the second-harmonic generation (SHG) and the difference-frequency generation (DFG) [22,23].

In this paper, the analysis is carried out in the frequency domain. A companion paper [28] investigates the evolution of the amplified pulses in time.

2. OPTICAL PARAMETRIC AMPLIFICATION IN NONUNIFORM QUASI-PHASE-MATCHING GRATINGS

A diagram illustrating OPA in nonuniform QPM gratings is shown in Fig. 1. We consider three copropagating waves, the pump, the signal, and the idler, with frequencies ω_p, ω_s, and ω_i, respectively. For their coupling to be most efficient, these three waves must satisfy the frequency-matching condition $\omega_p=\omega_s+\omega_i$. We denote by $\delta\omega\equiv\omega_s-\omega_{s0}$ the frequency shift of the signal wave with respect to a nominal frequency ω_{s0} and consider the pump frequency fixed for the present discussion. Due to the dispersive properties of the material, the three wavenumbers will not necessarily be matched [29]. We define $\Delta k(\delta\omega)\equiv k_p-k_s-k_i$ to be the intrinsic k-vector mismatch. In $\chi^{(2)}$ materials, perfect wave vector matching also maximizes the parametric gain.

The contribution of the QPM grating cancels most of the intrinsic wave vector mismatch. Here we consider rather general grating profiles. The only requirement that we impose on the grating period $\Lambda(z)$ is that it be a piecewise slow-varying function of position. We define $K_g(z)=2\pi/\Lambda(z)$ as the associated grating wavenumber. The overall wavenumber mismatch, κ, is the difference between the intrinsic mismatch and the potentially spatially nonuniform QPM grating:

$$\kappa(z,\delta\omega)=\Delta k(\delta\omega)-K_g(z). \tag{1}$$

The chirp rate $\kappa'(z)$ is the rate of change of the wavenumber mismatch in the axial direction:

$$\kappa'(z)=\frac{\partial\kappa(z,\delta\omega)}{\partial z}=-\frac{\mathrm{d}K_g(z)}{\mathrm{d}z}. \tag{2}$$

We define the perfect phase-match point (PPMP) to be at the position z_{pm} where $\kappa(z_{\mathrm{pm}},\delta\omega)=0$. The usual treatment of OPAs makes use of the slow-varying envelope approximation [29,30]. The frequency-domain signal and idler envelope functions $E_{s,i}(z,\pm\delta\omega)$ are obtained from the Fourier-domain representations of the electric fields $\tilde{E}_{s,i}(z,\omega_{s,i})$ by extracting their fast carrier phases, namely, $\tilde{E}_{s,i}(z,\omega_{s,i})=E_{s,i}(z,\pm\delta\omega)\exp[ik_{s,i}(\omega_{s,i})z]$. The wavenumbers $k_{s,i}(\omega_{s,i})$ introduced here are frequency-dependent; they account for material dispersion. [The conventional envelope description uses constant k-vectors for the envelopes, e.g., $\tilde{E}(z,\omega_{s,i})=E(z,\pm\delta\omega)\exp(ik_{s,i}z)$. The relationship between these two envelopes is discussed in more detail in [22].] We normalize the optical fields to make them proportional to the photon fluxes by introducing $A_{s,i}=(n_{s,i}/\omega_{s,i})^{1/2}E_{s,i}$, where $n_{s,i}$ are the refractive indices at the respective frequencies of the two waves. We treat the pump as an undepleted, monochromatic plane wave. The resulting steady-state rate equations for the spatial evolution of a pair of signal and idler frequency components are

$$\frac{\mathrm{d}A_s}{\mathrm{d}z}=i\gamma(z,\delta\omega)A_i^*e^{i\phi(z,\delta\omega)}, \tag{3}$$

$$\frac{\mathrm{d}A_i^*}{\mathrm{d}z}=-i\gamma(z,\delta\omega)A_se^{-i\phi(z,\delta\omega)}. \tag{4}$$

The coupling coefficient is $\gamma(z,\delta\omega)=(\omega_s\omega_i/n_sn_i)^{1/2}(d_{\mathrm{eff}}(z)/c)|E_p|$, where d_{eff} is the amplitude of the effective nonlinear coefficient of the QPM grating (i.e., the amplitude of the Fourier coefficient of the spatially modulated structure), $|E_p|$ is the magnitude of the pump wave electric field, and c is the speed of light in vacuum. We allow the coupling coefficient γ to vary slowly with position and frequency. The phase mismatch accumulated between the three waves is

$$\phi(z,\delta\omega)=\int_{z_0}^{z}\kappa(z',\delta\omega)\mathrm{d}z', \tag{5}$$

where z_0 is the position of the input plane of the grating. Finally, we will in general allow both signal and idler waves to be incident on the grating, with amplitudes $A_s(z_0,\delta\omega)=A_{s0}$ and $A_i(z_0,-\delta\omega)=A_{i0}$, respectively.

With the change of variables $A_{s,i}=a_{s,i}\gamma^{1/2}e^{i\phi/2}$, we combine the coupled-mode Eqs. (3) and (4) to eliminate one of the fields, leading to a second-order linear differential equation in standard form [31]:

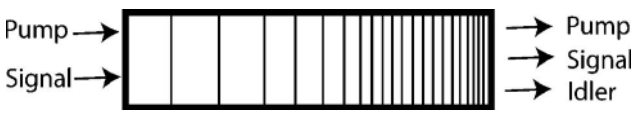

Fig. 1. Illustration of OPA in a chirped QPM grating.

$$\frac{d^2 a_{s,i}}{dz^2} + Q(z) a_{s,i} = 0, \tag{6}$$

where

$$Q(z) = \left(\frac{\kappa}{2} - \frac{i}{2}\frac{\gamma'}{\gamma}\right)^2 - \gamma^2 + \frac{i\kappa'}{2} + \frac{1}{2}\left(\frac{\gamma'}{\gamma}\right)', \tag{7}$$

and where prime denotes differentiation with respect to z.

The solutions to Eq. (6) will have an oscillatory character when $\mathrm{Re}(Q) > 0$ and will be exponentials when $\mathrm{Re}(Q) < 0$. The two regimes are separated by the turning points, given by the condition $1/2|\kappa| \approx \gamma$ (here we assume that γ'/γ is small and can be neglected). Located on either side of the PPMP, the turning points define the limits of the amplification region. A typical grating profile $\kappa(z,\omega)$ is shown in Fig. 2, together with the location of the PPMP and the two turning points, which define the extent of the amplification region.

3. PRACTICAL FORMULAS FOR OPTICAL PARAMETRIC AMPLIFICATION DESIGN

A. Wentzel–Kramers–Brillouin Solution

We use the WKB formalism and notation developed by Heading [32]. In this notation, the end points of the phase integrals as well as the order of dominance of the solutions are easily conveyed. We set the phase reference level at one of the complex turning points, where the function Q vanishes. Two such turning points exist, z_{tp1} and z_{tp2}, located in the complex plane on the left- and right-hand sides of the PPMP, respectively (see Appendix B, Fig. 11). The general WKB solutions using the left-hand-side turning point z_{tp1} as the phase reference level are written as

$$(z_{tp1}, z) \equiv Q^{-1/4}(z) \exp\left(i \int_{z_{tp1}}^{z} Q^{1/2}(z')\,dz'\right), \tag{8}$$

$$(z, z_{tp1}) \equiv Q^{-1/4}(z) \exp\left(i \int_{z}^{z_{tp1}} Q^{1/2}(z')\,dz'\right). \tag{9}$$

A linear combination of these two expressions defines approximate solutions that are valid away from the turning points. The "complex WKB method" consists of finding the linear combination of the general solutions that satisfy the boundary conditions in a given region and then in extending this solution to the entire complex plane by finding the coefficients that ensure continuity (asymptotically) between adjacent regions [32–34]. The details of the calculation are shown in Appendix B and C; here we only state the result. The signal at the end of the grating z_L is

$$A_s(z_L) \approx \left[\frac{\gamma(z_L)}{\gamma(z_0)}\right]^{1/2} e^{i\phi(z_L)/2}(C_+ - iC_-) i[z_{tp2}, z_{tp1}][(z_L, z_{tp2}) - i(z_{tp2}, z_L)], \tag{10}$$

with

$$C_+ = \frac{1}{(z_{tp1}, z_0)}\left[\left(1 + \frac{\gamma^2(z_0)}{\kappa^2(z_0)}\right) A_{s0} - \frac{\gamma(z_0)}{\kappa(z_0)} A_{i0}^*\right], \tag{11}$$

$$C_- = \frac{1}{(z_0, z_{tp1})}\left[-\frac{\gamma^2(z_0)}{\kappa^2(z_0)} A_{s0} + \frac{\gamma(z_0)}{\kappa(z_0)} A_{i0}^*\right], \tag{12}$$

$$[z_{tp2}, z_{tp1}] \equiv \exp\left(i \int_{z_{tp2}}^{z_{tp1}} Q^{1/2}(z)\,dz\right). \tag{13}$$

As mentioned before, z_0 is the position of the input plane and z_{tp1} and z_{tp2} are the turning points such that $Q(z_{tp1,2}) = 0$. The frequency argument has been suppressed to simplify the notation.

The factor $C_+ - iC_-$ together with the phase term $e^{i\phi/2}$ represent the contribution of the portion of grating located before the amplification region where the waves propagate, accumulate a relative delay and are combined before entering the amplification region. The factor $i[z_{tp2}, z_{tp1}]$ is the contribution from the amplification region where the waves grow with little phase accumulation. Propagation over the remaining portion of the grating is given by $(z_L, z_{tp2}) - i(z_{tp2}, z_L)$.

B. Design Formulas for a Single PPMP

We can simplify Eq. (10) further by retaining only its most significant contributions. An adequate approximation (derived in Appendix F) is given by

$$A_s \approx R(A_{s0} + iA_{i0}^* e^{i\varphi(z_0, z_{pm})}) e^{g(z_{tp1}, z_{tp2})}, \tag{14}$$

with $R = [\gamma(z_L)/\gamma(z_0)]^{1/2}$. The phase integral is

$$\varphi(z_0, z_{pm}) \equiv \int_{z_0}^{z_{pm}} \kappa(z)\,dz, \tag{15}$$

and the gain integral is

$$g(z_{tp1}, z_{tp2}) \equiv \int_{z_{tp1}}^{z_{tp2}} (\gamma^2 - \kappa^2/4)^{1/2}\,dz, \tag{16}$$

where the integration is carried out between the two turning points z_{tp1} and z_{tp2}.

Equation (14) is the central result of this paper. It is the basis of the design procedure explained below. It will be used repeatedly in several examples.

In a majority of cases we can linearize the grating profile around the PPMP. The amplification factor $G = e^g$ then becomes

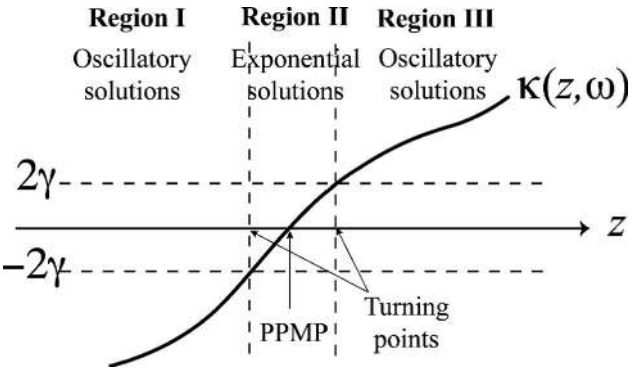

Fig. 2. Nonuniform grating profile showing the PPMP, the turning points, and the nature of the solutions in each region.

$$G_{\text{linear}} = \exp\left(\frac{\pi\gamma^2(z_{\text{pm}})}{|\kappa'(z_{\text{pm}})|}\right), \tag{17}$$

where the chirp rate and the coupling coefficient are evaluated at the PPMP. This is the Rosenbluth amplification formula [27], an important result first obtained in the context of laser–plasma interactions. For polynomial profiles the gain is given in terms of beta functions [24]. In particular, a case that we will be using later is the cubic profile $\kappa=\kappa'''(z-z_{\text{pm}})^3$, for which

$$G_{\text{cubic}} = \exp\left[\left(\frac{2\gamma^4(z_{\text{pm}})}{|\kappa'''|}\right)^{1/3}\int_{-1}^{1}\sqrt{1-u^6}\,\mathrm{d}u\right], \tag{18}$$

with $\int_{-1}^{1}(1-u^6)^{1/2}\mathrm{d}u=\frac{1}{3}\beta(\frac{1}{6},\frac{3}{2})\approx 1.82$.

C. Design Formulas for Multiple PPMPs

When a profile contains multiple PPMPs, the output of each monotonic segment becomes the input of the next. This situation is illustrated in Fig. 3.

A subtlety arises because the phase mismatch at the input of a given segment is not zero but results from the phase accumulation over the previous segments. This problem can be solved by absorbing the accumulated phase into the fields, i.e., letting $A_{s,i}^{(j)}=B_{s,i}^{(j)}e^{i\phi^{(j)}/2}$, where the superscripts refer to the segment number, and $\phi^{(j)}\equiv\int_{z_0^{(1)}}^{z_0^{(j)}}\kappa(z)\mathrm{d}z$ is the phase mismatch accumulated before segment j. Then the new fields obey the coupled-mode Eqs. (3) and (4) with initial conditions $B_{s,i0}^{(j)}=A_{s,i0}^{(j)}e^{-i\phi^{(j)}/2}$, and we can use the results derived above. Consequently, the contribution of a segment j can be written

$$A_s^{(j)} = R^{(j)}[A_{s0}^{(j)} + iA_{i0}^{(j)*}e^{i\varphi(z_0^{(1)},z_{\text{pm}}^{(j)})}]e^{g(z_{\text{tp1}}^{(j)},z_{\text{tp2}}^{(j)})}, \tag{19}$$

$$A_i^{(j)} = R^{(j)}[A_{i0}^{(j)} + iA_{s0}^{(j)*}e^{i\varphi(z_0^{(1)},z_{\text{pm}}^{(j)})}]e^{g(z_{\text{tp1}}^{(j)},z_{\text{tp2}}^{(j)})}. \tag{20}$$

In the case of periodic profiles, $A_{s0}^{(j)}=A_s^{(j-1)}$, $A_{i0}^{(j)}=A_i^{(j-1)}$. However, when multiple gratings are used in a cascaded configuration this is not necessarily the case. A typical example is the tandem configuration discussed in Subsection 4.E.

4. ANALYSIS OF VARIOUS GRATING PROFILES

This section illustrates the engineering of chirped gratings. We first review the well-known case of a uniform QPM grating. Then, we examine the linear profile, which essentially yields constant gain over a large bandwidth, and we also examine ways of eliminating the ripple affecting the spectrum. Then, as an example of nonuniform chirp rate we discuss a sinusoidal modulation superposed onto a linear ramp providing enhanced amplification at selected frequencies. Finally, we examine a tandem design for simultaneous gain and group delay control.

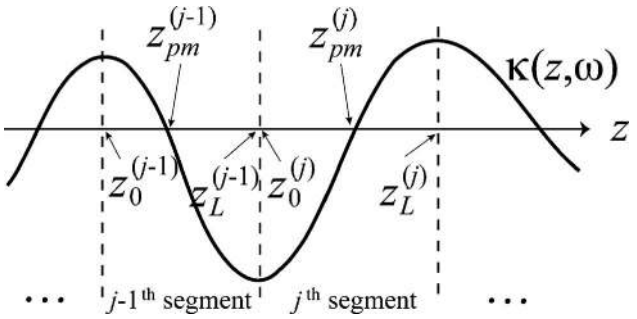

Fig. 3. Grating profile with multiple PPMPs.

A. Uniform Profile

In the case of a uniform QPM grating, there are no turning points since the wave vector mismatch κ is constant, and as a consequence the nature of the solutions (i.e., real or complex exponentials) remains unchanged throughout the medium. The WKB analysis developed herein does not apply in this simple case.

When the wave vector mismatch κ and the coupling coefficient γ are constant, the coupled Eqs. (3) and (4) can be solved exactly [29,30]:

$$A_s(z_L) = A_{s0}e^{i\kappa L/2}\left[\cosh\Gamma L - \frac{i\kappa}{2\Gamma}\sinh\Gamma L\right] + i\frac{\gamma}{\Gamma}A_{i0}^{*}e^{i\kappa L/2}\sinh\Gamma L, \tag{21}$$

$$A_i(z_L) = A_{i0}e^{i\kappa L/2}\left[\cosh\Gamma L - \frac{i\kappa}{2\Gamma}\sinh\Gamma L\right] + i\frac{\gamma}{\Gamma}A_{s0}^{*}e^{i\kappa L/2}\sinh\Gamma L, \tag{22}$$

where $L=z_L-z_0$ is the length of the grating and

$$\Gamma = \sqrt{\gamma^2-\left(\frac{\kappa}{2}\right)^2} \tag{23}$$

is the growth rate in the presence of constant wave vector mismatch. With input at the signal wave only and in the large-gain regime ($\Gamma L\gg 1$), the amplitudes of the waves are approximately

$$|A_{s,i}(z_L)| \approx A_{s0}\frac{\gamma}{2\Gamma}e^{\Gamma L}. \tag{24}$$

The peak gain, achieved when $\kappa=0$, is

$$G_{\text{uniform}} = \frac{1}{2}e^{\gamma L}. \tag{25}$$

The gain increases exponentially with the length of the device. The FWHM bandwidth is reached when the wave vector mismatch is equal to

$$\kappa_{\text{FWMH}} = \pm\frac{2}{L}\sqrt{\gamma^2L^2-(\ln 2)^2}. \tag{26}$$

The amplification bandwidth takes a simple form if we neglect group-velocity dispersion at the signal and idler wavelengths and assume off-degenerate operation. In this case, the intrinsic wave vector mismatch is

$$\Delta k(\delta\omega) = k_p - k_s - k_i$$
$$\approx k_p - k_{s0} - \left.\frac{\partial k}{\partial \omega}\right|_{\omega_{s0}} \delta\omega - k_{i0} + \left.\frac{\partial k}{\partial \omega}\right|_{\omega_{i0}} \delta\omega$$
$$= k_p - k_{s0} - k_{i0} + \left(\frac{1}{v_s} - \frac{1}{v_i}\right)\delta\omega, \tag{27}$$

where k_{s0} and k_{i0} are the signal and idler wave vectors at the nominal frequencies and $v_{s,i} = \partial\omega/\partial k|_{\omega_{s0,i0}}$ are the group velocities. The grating wave vector is equal to $K_g = k_p - k_{s0} - k_{i0}$ (by definition of the nominal frequencies), so that the overall mismatch, given by Eq. (1), is simply

$$\kappa(\delta\omega) = \left(\frac{1}{v_s} - \frac{1}{v_i}\right)\delta\omega. \tag{28}$$

We define the group-velocity mismatch parameter, δv, as

$$\frac{1}{\delta v} \equiv \frac{1}{v_s} - \frac{1}{v_i}. \tag{29}$$

Substituting into Eq. (26), we find the following expression for the FWHM bandwidth:

$$\Delta\omega_{\text{uniform}} = \frac{4|\delta v|}{L}\sqrt{\gamma^2 L^2 - (\ln 2)^2} \approx 4|\delta v|\gamma, \tag{30}$$

where the approximation is valid in the large-gain regime. Therefore the bandwidth of a uniform QPM grating in the high-gain limit is essentially independent of the grating length. It depends only on the strength of the coupling coefficient and on the dispersive properties of the material.

B. Linear Profile for Broadband Amplification

1. Application of the Design Formula

The most basic chirped QPM grating profile is the linear chirp. We consider an input signal wave only, as this is the most common situation in practice and let the idler develop from the interaction. For simplicity, we neglect group-velocity dispersion at the signal and idler wavelengths so that the phase mismatch varies linearly with frequency. (The extension to higher-order dispersion is straightforward if somewhat more tedious.) The total wave vector mismatch, Eq. (1), is given by

$$\kappa(z, \delta\omega) = \kappa'(z - z_{\text{pm0}}) - \frac{\delta\omega}{\delta v}, \tag{31}$$

where κ' is the constant chirp rate and z_{pm0} is the position of the PPMP at the nominal frequency. As the input frequency is varied, the PPMP is shifted linearly with frequency according to

$$z_{\text{pm}} = z_{\text{pm0}} + \frac{\delta\omega}{\kappa'\,\delta v}. \tag{32}$$

The mismatch then takes the simple form

$$\kappa = \kappa'(z - z_{\text{pm}}). \tag{33}$$

The two turning points are located at a distance given by $2\gamma/|\kappa'|$ on each side of the PPMP; therefore the length of the amplification region is

$$L_g = \frac{4\gamma}{|\kappa'|}. \tag{34}$$

The present approximate treatment is valid for gratings for which $L \gg L_g$. If this condition is satisfied, then the dephasing effects due to the chirp of the grating dominate the behavior of the device. Conversely, if $L \ll L_g$, then the grating is essentially uniform.

The limits of the amplification spectrum are reached when the frequency shift results in one of the turning points being at the edge of the grating. Therefore the amplification bandwidth is

$$\Delta\omega_{\text{chirped}} = |\kappa'\,\delta v|(L - L_g). \tag{35}$$

As expected, the bandwidth is proportional to the product of the chirp rate and the grating length, i.e., to the range of grating k-vectors in the device. The bandwidth takes this simple form when the group-velocity dispersion of the material can be neglected. Otherwise, higher dispersive orders have to be included in Eq. (31), and the bandwidth may have to be calculated directly from the dispersion relation, as discussed in [26].

The application of Eq. (14) for each wave gives

$$A_s = A_{s0} e^{\pi\gamma^2/|\kappa'|}, \tag{36}$$

$$A_i = iA_{s0}^* e^{\pi\gamma^2/|\kappa'|} e^{-i\kappa'(z_{\text{pm}} - z_0)^2/2}. \tag{37}$$

Both waves experience the constant amplitude gain given by the Rosenbluth gain formula:

$$G_{\text{Rosenbluth}} = e^{\pi\gamma^2(\delta\omega)/|\kappa'|}. \tag{38}$$

However, they differ in their phases. While the signal experiences negligible phase shift, the idler accumulates a quadratic phase corresponding to a time delay (with respect to a reference traveling at the idler velocity) of

$$\tau_i = \frac{z_{\text{pm}} - z_0}{\delta v}. \tag{39}$$

Since this delay is linear itself in the input frequency [through its dependence on $z_{\text{pm}}(\delta\omega)$], the idler experiences group delay dispersion, the magnitude of which depends on the chirp rate. Alternatively, the idler group delay with respect to the corresponding signal wave Fourier component is

$$\tau_{i-s} = -\frac{z_L - z_{\text{pm}}}{\delta v}. \tag{40}$$

It is important to keep in mind that these phases represent the contribution from the grating only; the dispersive properties of the material must be considered separately. They are accounted for by the carrier phase $k_{s,i}z - \omega_{s,i}t$, which must be added to the envelopes in order to

recover the Fourier representation of the fields. Material dispersion is in fact buried in the wave vectors $k_{s,i} = \omega_{s,i} n(\omega_{s,i})/c$.

2. Comparison with Wentzel–Kramers–Brillouin Solution

The approximate design formulas lead to simple expressions for the gain, bandwidth, and phase. It is natural to expect that this simplicity comes at the price of a loss of accuracy. The accuracy of our expressions can be verified by comparing it with the fuller WKB and numerical solutions.

The WKB solution, Eq. (10), is valid for general grating profiles. In Appendix E, we obtain an explicit expression in the special case of a linear profile [see Eq. (E7)]. The spatial evolution of the waves is plotted in Fig. 12 along with the numerical solution. The underlying assumptions behind the WKB solution are also discussed there.

Figure 4 compares the gain spectra obtained from the explicit WKB solution, Eq. (E7), with the numerical solution, together with the simplified result obtained in Subsection 4.B.1, Eqs. (36) and (37). Figure 5 shows the phase spectra. The signal has a small phase drift that is not captured by the simplified expressions. However, the idler has a large quadratic spectral phase predicted by Eq. (37). Finally, Fig. 6 shows the relative group delay, τ, with respect to the input signal. As expected, the idler experiences a linear group delay, reflecting the linear relationship between the position of the PPMP and frequency.

A striking feature of those plots is the significant ripple on the gain, phase, and group delay spectra. While the WKB solution in Eq. (10) recovers this ripple correctly, the small-scale features of the amplification are lost when making the simplifications leading to the design formula in Eq. (14). The origins of the ripple and the ways to reduce it will be discussed in Section 5.

Figure 6 indicates that the magnitude of the group delay ripple is typically of the order of 10% of the delay accumulated between the signal and idler, and that it decreases with an increasing chirp rate or increasing length. For femtosecond pulse amplification, the pulse distortion resulting from this group delay ripple is often unacceptable.

3. Comparison with Uniform Gratings

From the point of view of applications, the clear advantage of linearly chirped QPM gratings lies in their arbitrarily wide amplification bandwidth. For a fixed grating length, the bandwidth is essentially proportional to the chirp rate κ'. Naturally, an increase of bandwidth comes at the expense of a reduction of gain since the Rosenbluth factor is proportional to $1/\kappa'$. The trade-off between gain and bandwidth is expressed by the fact that the logarithmic-gain-bandwidth product is a quantity independent of the chirp rate:

$$\ln G_{\text{Rosenbluth}} \times \Delta\omega_{\text{chirped}} \approx \pi |\delta v| \gamma^2 L. \tag{41}$$

In the case of a uniform grating, the peak gain and the amplification bandwidth are given by Eqs. (25) and (30), respectively. The logarithmic-gain-bandwidth product in this case is approximately

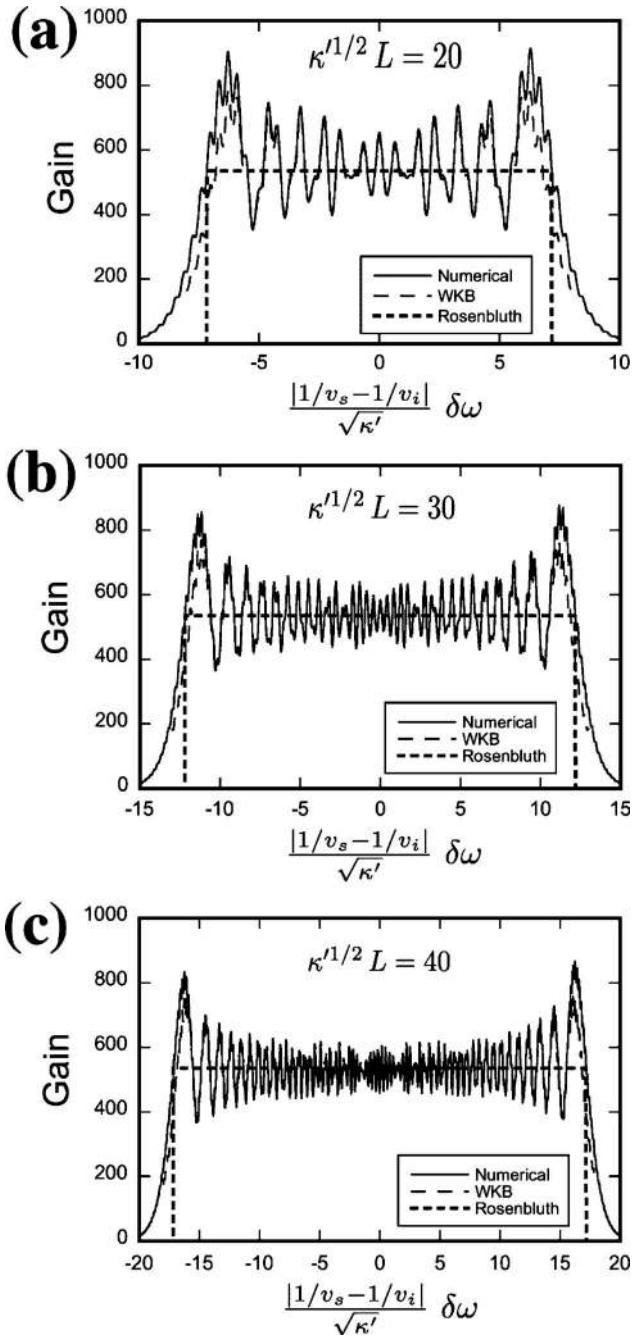

Fig. 4. Gain spectrum of a linear profile comparing the numerical solution with the WKB solution and the Rosenbluth gain factor for various grating lengths. The numerical values used are $\gamma^2/\kappa' = 2$ and (a) $\kappa'^{1/2} L = 20$, (b) $\kappa'^{1/2} L = 30$, and (c) $\kappa'^{1/2} L = 40$.

$$\ln G_{\text{uniform}} \times \Delta\omega_{\text{uniform}} \approx 4 |\delta v| \gamma^2 L. \tag{42}$$

The logarithmic-gain-bandwidth products of uniform and chirped gratings are essentially the same (except for a factor of 4 instead of π).

The advantages of chirped gratings over uniform gratings are to enable (in principle) arbitrarily large bandwidths and to allow shaping of the gain and group delay spectra. However, this increase of bandwidth is accompanied by a reduction of the gain, according to Eq. (41).

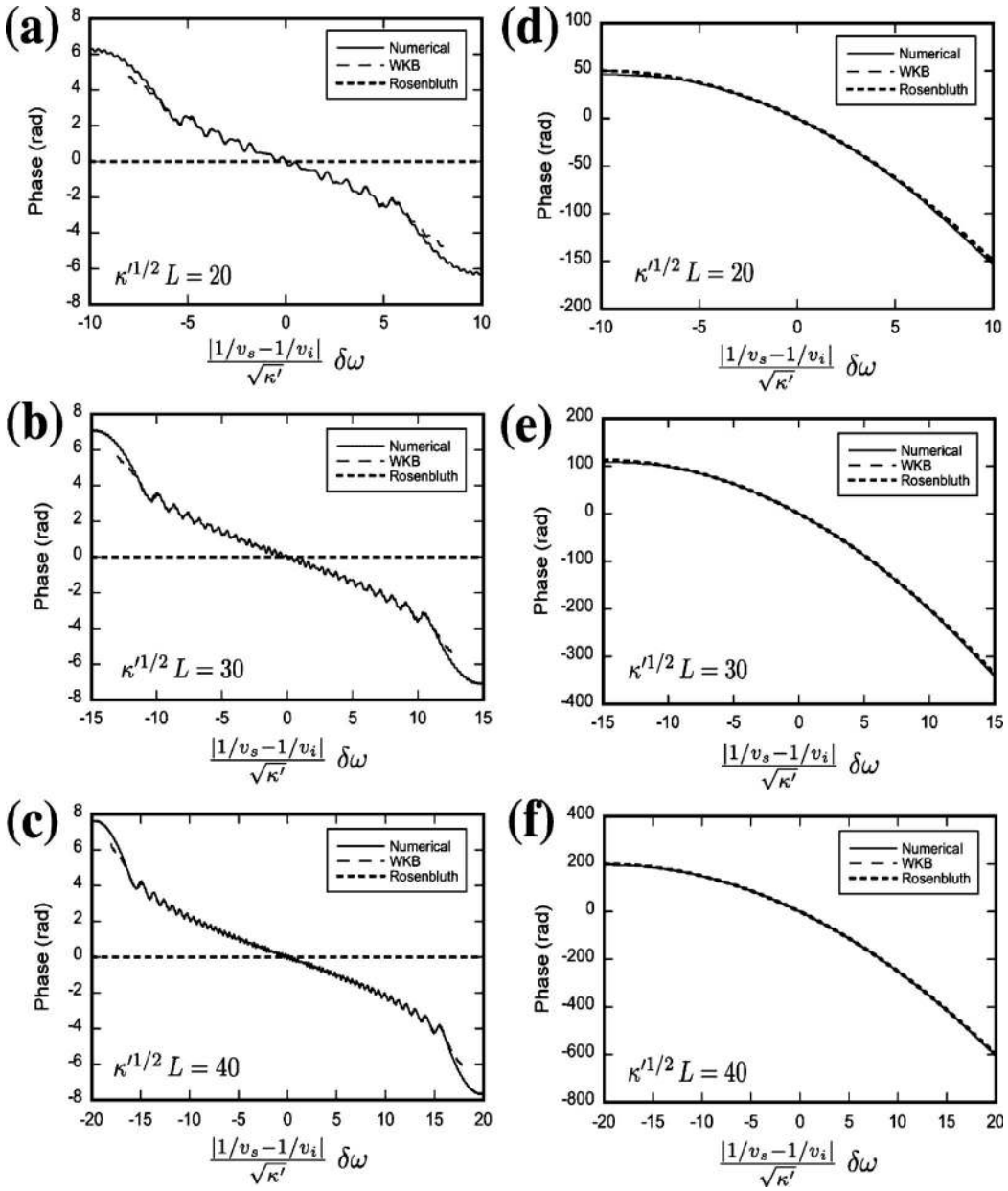

Fig. 5. Phase spectrum of a linear profile comparing the numerical solution with the WKB solution and the simplified expressions, Eqs. (36) and (37), for various grating lengths. Plots (a)–(c) correspond to the signal, plots, (d)–(f) correspond to the idler. The numerical values used are $\gamma^2/\kappa' = 2$ and (a), (d) $\kappa'^{1/2}L = 20$; (b), (e) $\kappa'^{1/2}L = 30$; and (c), (f) $\kappa'^{1/2}L = 40$.

4. Concrete Design Example

To give an idea of typical experimental values, let us consider an OPA consisting of a chirped QPM grating designed to offer a (power) gain of 50 dB over a bandwidth of 100 nm ~ 1550 nm. The nonlinear crystal is made of periodically poled lithium niobate (PPLN) and has a length of 5 cm. We assume that the OPA is pumped by a Nd:YAG laser (1064 nm). The numerical values of the various experimental parameters involved are listed in Table 1. The chirp rate required is $\kappa' = 4.13 \times 10^5\ \mathrm{m}^{-2}$. To obtain the desired gain, the coupling coefficient must be $\gamma = 870\ \mathrm{m}^{-1}$. The required pump intensity to achieve this is $438\ \mathrm{MW/cm}^2$. In terms of normalized quantities, the gain parameter is $\gamma^2/\kappa' = 1.8$, and the length is $\kappa'^{1/2}L = 32$. This situation is very similar to the one illustrated in Fig. 4(b).

By comparison, the pump intensity required to achieve the same gain in a uniform grating of equal length is $7.6\ \mathrm{MW/cm}^2$. However, in this case the bandwidth is ~6 nm only. The 1D model studied here assumes that the pump, signal, and idler are plane waves. In a free-space experiment, however, the light pulses are localized in space and time. A reasonable approximation (neglecting diffraction and dispersion) is to average the gain over the entire pulse:

$$G_{3D} = \int\int\int \exp\left(\frac{\pi\gamma^2(x,y,t)}{|\kappa'|}\right) \mathrm{d}x\mathrm{d}y\mathrm{d}t, \qquad (43)$$

where now the coupling coefficient has a transverse and temporal profile related to the intensity of the pump

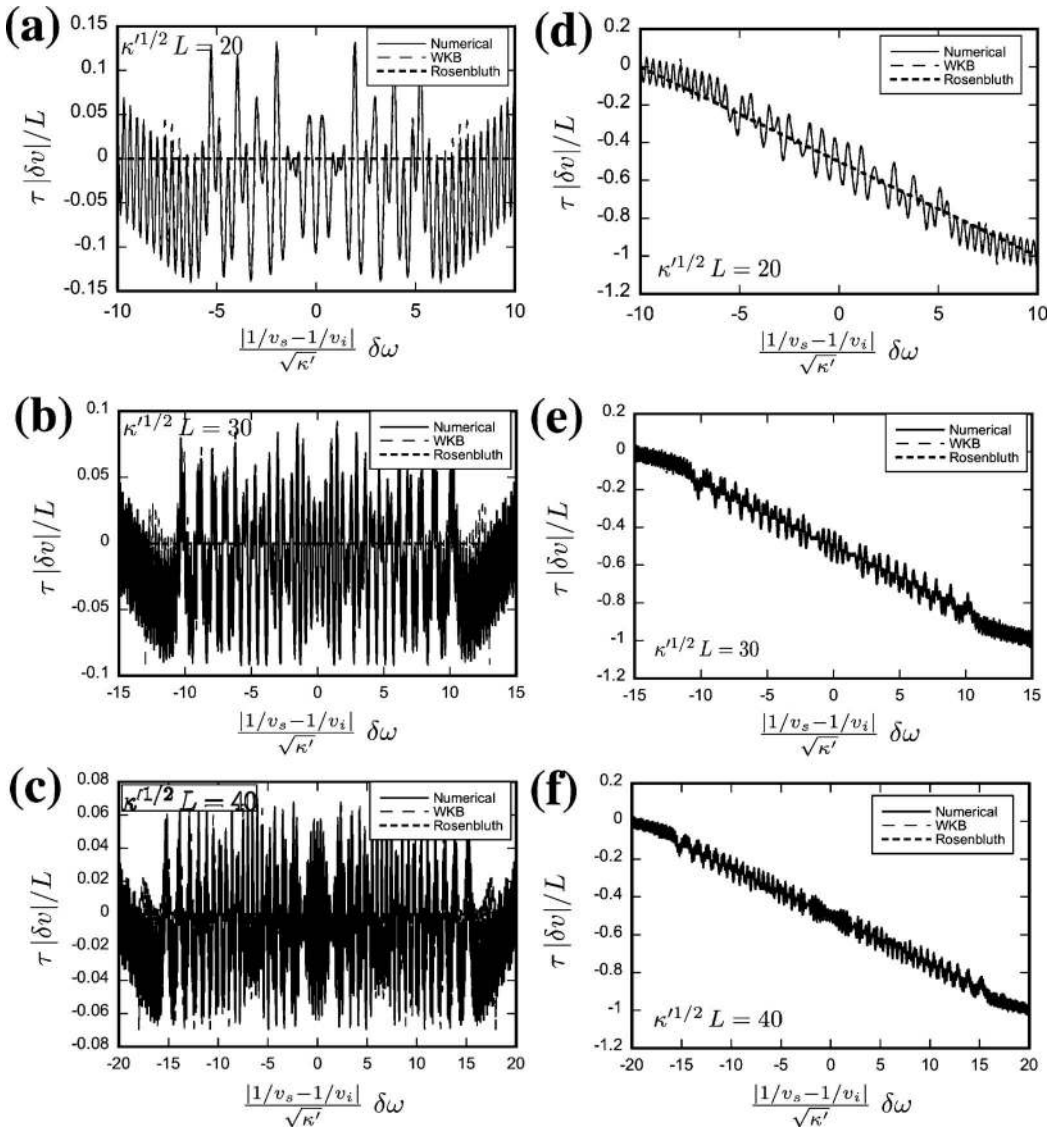

Fig. 6. Group delay spectrum of a linear profile normalized with respect to the delay between the waves $\tau/|1/v_s - 1/v_i|L = \tau|\delta v|/L$. The delays are relative to reference waves traveling at the signal and idler velocities, respectively. These plots compare the numerical solution with the WKB solution and the simplified expressions, Eqs. (36) and (37), for various grating lengths. Plots (a)–(c) correspond to the signal, plots (d)–(f) correspond to the idler. The numerical values used are $\gamma^2/\kappa' = 2$ and (a), (d) $\kappa'^{1/2}L = 20$; (b), (e) $\kappa'^{1/2}L = 30$; and (c), (f) $\kappa'^{1/2}L = 40$.

pulse, $\gamma^2(x,y,t) \propto I_p(x,y,t)$. If we assume that the pump pulses are Gaussian in space and time with a spot size of 300 μm ($1/e^2$ intensity diameter) and a duration of 1 ns ($1/e^2$ intensity full duration) but the same peak intensity as the plane wave example just given, then the gain of the OPA is 35 dB instead of 50 dB. Diffraction, inevitable when gain narrowing occurs, will decrease this value even further.

5. Comparison with Noncollinear Phase Matching

As mentioned in Section 1, a common way of broadening the amplification bandwidth of OPAs is to use a noncollinear geometry [11]. This technique consists of introducing an angle between the signal and the pump beams and in spatially dispersing the input signal, so that at each frequency component the signal group velocity is equal to the projection of the idler group velocity along the signal direction. This approach effectively cancels the group-velocity mismatch between the two waves. Consequently, the bandwidth is limited not by group-velocity dispersion but by higher dispersive orders in a manner similar to a degenerate OPA.

The drawback of noncollinear phase matching is that spatial walk-off limits the gain length of the amplifier. Assuming a pump beam of a width $2w_0$ and a noncollinear angle α between the pump and signal beams, the effective gain length is approximately $L_{\text{eff}} \approx 2w_0/\tan\alpha$.

By comparison, chirped QPM gratings do not attempt to correct for group-velocity mismatch. Instead, they offer a broad range of phase-matching periods. Since they operate in a collinear geometry, spatial walk-off does not limit the gain length. Other major advantages of chirped QPM OPAs are the possibility of engineering the gain and group delay spectra. Their drawback is that, unlike with the noncollinear phase-matching technique, there exist a trade-off between gain and bandwidth.

Table 1. Numerical Values for the OPA Design

Specifications	
Material	$LiNbO_3$
Center signal wavelength	1550 nm
Bandwidth	100 nm
Pump wavelength	1064 nm
Grating length, L	5 cm
Power gain	50 dB
Operating temperature	150 °C
QPM Grating	
QPM grating period range	28.3–31.2 μm
Chirp rate, κ'	4.13×10^5 m^{-2}
Normalized length, $\sqrt{\kappa'}L$	32
Pump Intensity	
Effective nonlinear coefficient, d_{eff}	$2/\pi\times27$ pm/V
Coupling coefficient, γ	870 m^{-1}
Gain parameter, γ^2/κ'	1.83
Gain length, L_g	8.4 mm
Pump intensity	438 MW/cm^2

Since the performance of each approach depends on different physical quantities (e.g., high-order dispersive orders in the case of noncollinear phase matching and the available grating length in the case of chirped QPM OPAs), it is impossible to assert in an absolute manner which approach is best. We can work out an example based on the experimental conditions reported in [35]. The authors report a noncollinear OPA in periodically poled lithium tantalate. They use a pump laser at 785 nm with a spot size of 180 μm to achieve gain over a bandwidth ranging from 1.1 to 1.6 μm. Material dispersion at those wavelengths imposed a noncollinear angle $\alpha\approx2°$. Consequently, spatial walk-off limits the effective gain length to $L_{\text{eff}}\approx5.2$ mm. We will assume that the power gain is given as in the case of a uniform medium by $G=\exp 2\gamma L_{\text{eff}}$. Then, in order to achieve, for instance, a gain of 40 dB, the required coupling coefficient is $\gamma\approx893$ m^{-1}. Let us now calculate the gain obtained by the same pump beam in a chirped QPM OPA assuming a grating length of 5 cm. Neglecting high-order dispersion, the chirp rate required to achieve the desired bandwidth, given by Eq. (35), is $\kappa'\approx8.8\times10^5$ m^{-2}. The Rosenbluth gain parameter is then $\gamma^2/\kappa'\approx1.65$, corresponding to a power amplification of 45 dB.

In the example given above, the performances of the two techniques are similar. Chirped QPM OPAs would become advantageous if the grating length were increased. On the other hand, noncollinear OPAs would perform better if the material were less dispersive.

C. Tapered Profiles for Ripple Reduction

The gain, phase, and group delay ripple affecting the amplification spectrum of chirped gratings can be relatively large. Subsection 4.C explores ways of reducing the ripple by tapering the magnitude of the coupling coefficient or the grating profile.

The ripple is due to the fact that some amount of idler wave is generated before reaching the gain region. When they reach the phase-matching region, contributions from the signal and idler are superposed, and their relative phase affects the magnitude of the gain.

This phenomenon can be understood using the WKB description. The solution is constructed by the superposition of the two elementary WKB solutions given by Eqs. (8) and (9). These positive and negative complex exponentials interfere, causing small oscillations in the signal and idler amplitudes.

From a physical point of view, the ripple is caused by the "hard" edges of the grating where the interaction is turned on and off abruptly. Therefore, ripple reduction schemes should aim at making the transition into and out of the interaction region as smooth as possible. There are two ways of accomplishing this. One way is to turn on the coupling coefficient adiabatically; the other consists of starting from a completely mismatched interaction that is then brought progressively into phase matching.

Tapering of the coupling coefficient $\gamma(z)$ can be accomplished, for example, by varying the duty cycle of the QPM grating or by omitting domain reversals [36]. For instance, let us consider the profile:

$$\frac{\gamma(z)}{\gamma_{\max}}=a+b\times\tanh\left(\frac{z-z_0-l_1}{w_1}\right)\times\tanh\left(\frac{L-z+z_0-l_2}{w_2}\right). \tag{44}$$

The various constants can be chosen to achieve satisfactory ripple reduction. The Rosenbluth gain factor is now frequency-dependent with $\gamma=\gamma[z_{\text{pm}}(\delta\omega)]$ and $z_{\text{pm}}(\delta\omega)$ given by Eq. (32). The reduction of the gain at the edges of the spectrum causes a narrowing of the amplification bandwidth. Figure 7 shows the tapering function and the corresponding amplification and group delay spectra. For this particular bandwidth and gain, the amplitude of the gain ripple could be reduced from ~100% of the average gain (peak-to-peak variation) to 2% with the parameters $l_1=l_2=w_1=w_2=0.04\times L$ and a and b chosen so that $\gamma(z_0)=\gamma(z_L)=0$ and $\max\gamma(z)=\gamma_{\max}$.

Let us now turn our attention to the tapering of the phase mismatch profile of the grating, $\kappa(z)$. As an example, we consider a profile that is linear for most of the grating, but becomes large at the ends. This is accomplished for instance by adding a large, odd power to the linear grating profile:

$$\kappa=\kappa_0'(z-z_{\text{pm0}})+\mu\left(\frac{z-z_{\text{pm0}}}{L/2}\right)^{\nu}-(1/v_s-1/v_i)\delta\omega, \tag{45}$$

where μ is the amplitude of the departure from linearity and ν is a large, odd integer. The Rosenbluth amplification factor is now dependent on frequency through the nonuniform chirp rate $\kappa'=\kappa'[z_{\text{pm}}(\delta\omega)]$. The gain is reduced at the edges of the spectrum corresponding to regions of large chirp rate.

Figure 8 shows the grating profile and the corresponding amplification and group delay spectra. The amplitude of the ripple could be kept below 5% of the average gain using the parameters $\mu/\kappa_0'^{1/2}=100$ and $\nu=21$. These numerical results show that tapering of the coupling coeffi-

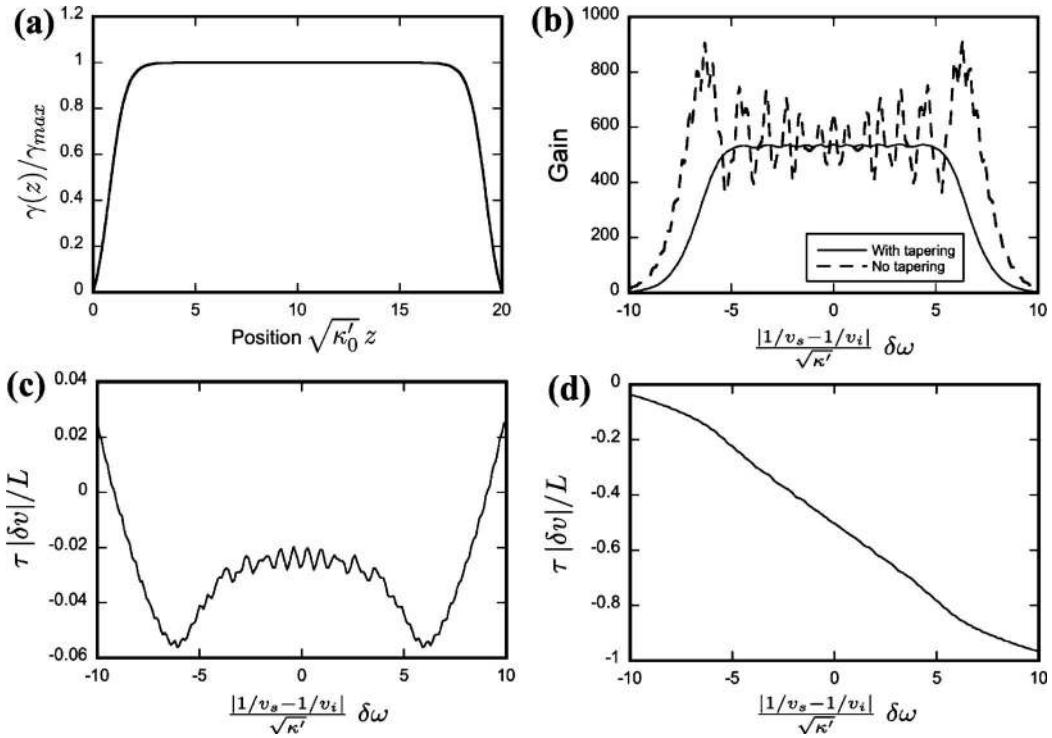

Fig. 7. Ripple reduction using tapering of the coupling coefficient: (a) coupling coefficient profile, (b) gain spectrum, (c) signal group delay spectrum, and (d) idler group delay spectrum. The group delays are defined with respect to reference waves traveling at the signal and idler velocities, respectively. The tapering profile is given by Eq. (44) with $l_1=l_2=w_1=w_2=0.04\times L$. The gain parameter is $\gamma^2/\kappa'=2$ and the length is $\kappa'^{1/2}L=20$. The gain and group delay spectra without apodization were shown in Figs. 4 and 6, top case.

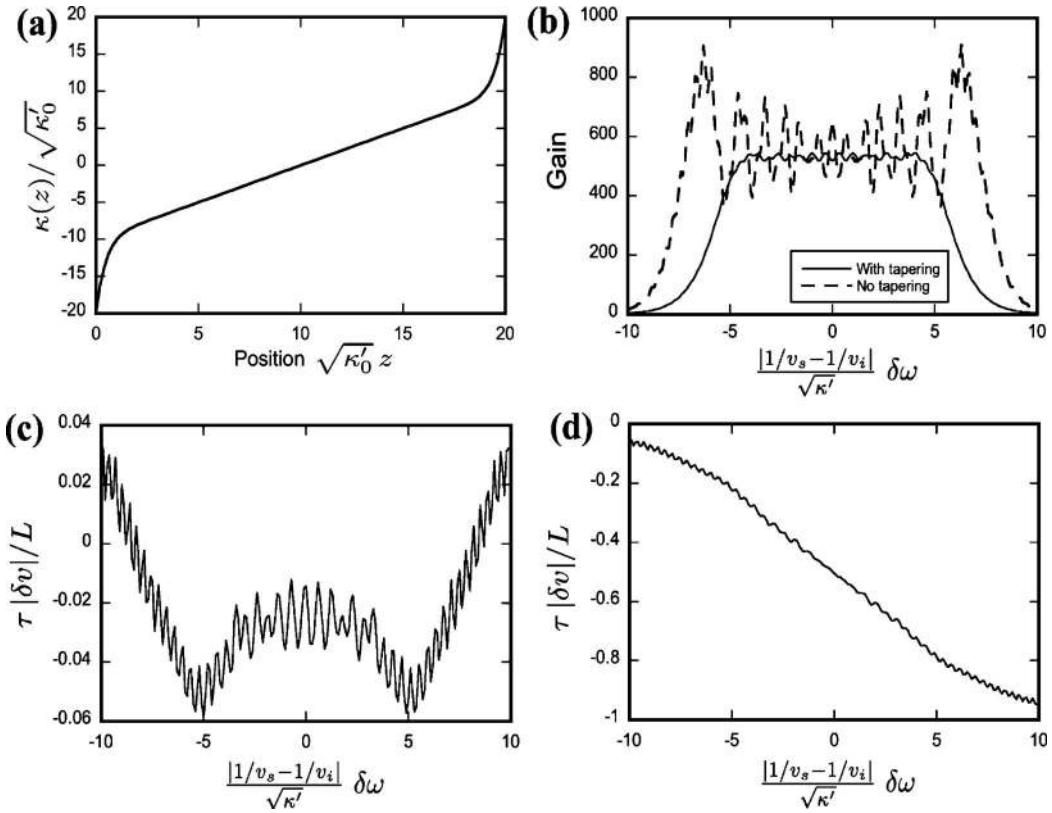

Fig. 8. Ripple reduction using tapering of the QPM profile: (a) grating profile, (b) gain spectrum, (c) signal group-delay spectrums and (d) idler group delay spectrum. The group delays are defined with respect to reference waves traveling at the signal and idler velocities, respectively. The grating profile is given by Eq. (45) with $\mu/\kappa_0'^{1/2}=100$ and $\nu=21$. The gain parameter is $\gamma^2/\kappa_0'=2$ and the length is $\kappa'^{1/2}L=20$.

cient seems more effective at eliminating the group delay ripple than tapering of the phase profile of the grating.

As a concrete example, we consider the design described in Subsection 4.B.4. To obtain a 100 nm wide amplification bandwidth, the QPM period must range from 28.3 to 31.2 μm over a length of 5 cm. Tapering of the QPM profile can be done by keeping ~90% of the central portion of the grating unchanged and by progressively increasing the chirp rate at the two ends so that the grating period reaches, for example, 25.3 μm at one end and 33.2 μm at the other.

D. Sinusoidal Profile for Selective Frequency Amplification

According to the design formulas, the amplification in the case of a monotonic profile with no input idler is simply e^g, where g is the gain integral given in Eq. (16). Thus the amplification depends predominantly on the local properties of the grating in the vicinity of the PPMP. This opens the possibility of engineering the amplification spectrum through careful design of the grating profile.

By way of illustration, we consider a sinusoidal modulation superposed onto a linear profile and show that it gives rise to an amplification spectrum with enhanced gain around certain frequencies only. Such a profile is described by

$$\kappa = \kappa_0'(z - z_{\mathrm{pm}0}) - \mu \sin[k_\mu(z - z_{\mathrm{pm}0})] - (1/v_s - 1/v_i)\delta\omega, \tag{46}$$

where μ and k_μ are the amplitude and spatial frequency of the modulation, respectively. If the amplitude of the modulation is small (i.e., $\mu k_\mu \ll \kappa_0'$), then the linearization of the profile is valid everywhere and the gain is obtained from the Rosenbluth formula using the frequency-dependent chirp rate $\kappa' = \kappa_0' - \mu k_\mu \cos k_\mu(z_{\mathrm{pm}} - z_{\mathrm{pm}_0})$, where z_{pm} is now the solution of the transcendental equation $\kappa(z_{\mathrm{pm}}) = 0$. However, as the amplitude of the modulation increases the chirp rate becomes close to zero at certain locations inside the grating. When $\mu k_\mu = \kappa_0'$ the profile can be approximated by a cubic at those locations where κ' vanishes, and in these cases we can use the gain formula in Eq. (18), which in our particular case becomes

$$G = \exp\left[4.17\left(\frac{\gamma^4}{\kappa_0' k_\mu^2}\right)^{1/3}\right]. \tag{47}$$

The amplification spectrum of this sinusoidal profile is shown in Fig. 9 for parameters $\gamma^2/\kappa_0' = 2$, $\kappa_0'^{1/2}L = 40$, $k_\mu = 2\pi/(L/3)$, and $\mu = \kappa_0'/k_\mu$. The minimum channel spacing that can be achieved with a sinusoidal profile is roughly equal to the bandwidth of a uniform QPM grating given by Eq. (30). It is typically of the order of a few nanometers.

Let us take as an example the design introduced in Subsection 4.B.4. We keep the same range of QPM periods, namely, 28.3–31.2 μm, and grating length (5 cm). The profile described in Fig. 9 is achieved by introducing a sinusoidal modulation such that the chirp rate reaches zero at three locations (0.83, 2.5, and 4.17 cm), corresponding to QPM periods of approximately 28.8, 29.8, and 30.8 μm.

E. Tandem Gratings for Simultaneously Flat Gain and Group Delay Spectra

The examples presented above illustrate how one can tailor the amplification spectrum through careful engineering of the grating profile. Little has been said about designing the phase response. Nevertheless, control of the phase spectrum is often critical, especially for applications in ultrafast optics.

Recently, we proposed the use of a pair of gratings in a tandem configuration in order to achieve simultaneous control of the gain and group delay spectra [26]. This idea of using the idler wave in a cascaded geometry has also been used to reduce the amplified spontaneous emission and improve the pulse contrast in high-gain OPAs [10]. Here is an analysis of this design using the simple design expressions. We will see that the equations governing the design procedure follow in a straightforward manner.

The tandem configuration is shown in Fig. 10. Its principle of operation is the following. The signal to be amplified is incident on the first grating. After the first grating, we block the signal wave so that only the pump and the idler are incident on the second grating. The output idler of the first grating is used as the input signal of the second. The "idler" generated by the second grating then has

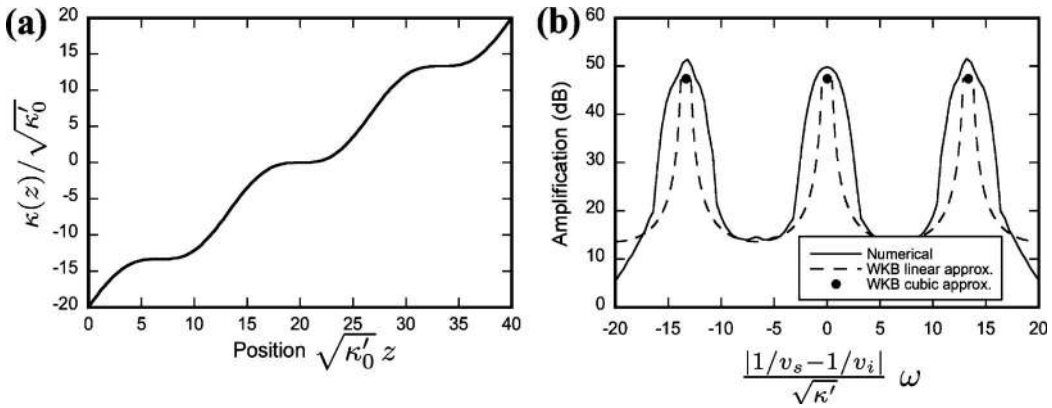

Fig. 9. Sinusoidal profile for selective frequency amplification: (a) QPM grating profile and (b) amplification spectrum, comparing the numerical values with the Rosenbluth amplification formula. The cubic approximation to the grating profile gives the peak amplification (marked by the dots on the plot), while the linear approximation (dashed curve) is valid away from the peaks but not in the vicinity of the maxima. The numerical parameters in this example are $\gamma^2/\kappa_0' = 2$, $\kappa_0'^{1/2}L = 40$, $k_\mu = 2\pi/(L/3)$, and $\mu = \kappa_0'/k_\mu$.

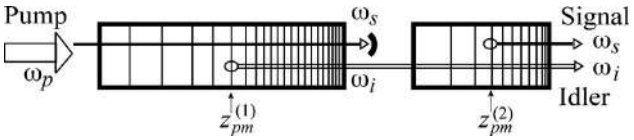

Fig. 10. Tandem configuration.

the same frequency as the original signal. By choosing the position of the PPMPs in the two gratings and their local chirp rates, we can control the gain and group delay spectra at the same time.

Let us now describe the output of the tandem-grating design. We use the expressions describing the amplification in the presence of multiple PPMPs, Eqs. (19) and (20), with $A_{i0}=0$. The output of the first grating is

$$A_s^{(1)} = R^{(1)} A_{s0} e^{g^{(1)}}, \tag{48}$$

$$A_i^{(1)} = iR^{(1)} A_{s0}^* e^{g^{(1)}} e^{i\varphi(z_0^{(1)}, z_{\mathrm{pm}}^{(1)})}, \tag{49}$$

where $g^{(1)}$ denotes the gain integral around the PPMP of the first grating [Eq. (16)]. For a locally linear chirp rate, $g^{(1)} = \pi\gamma(z_{\mathrm{pm}}^{(1)})/\kappa'(z_{\mathrm{pm}}^{(1)})$. Before entering the second grating, the signal is filtered out. The inputs to the second gratings are therefore $A_{s0}^{(2)}=0$, $A_{i0}^{(2)}=A_i^{(1)}$. A second application of Eq. (19) then gives

$$A_s^{(2)} = A_{s0}^* R^{(1)} R^{(2)} e^{g^{(1)}+g^{(2)}} e^{i\varphi(z_{\mathrm{pm}}^{(1)}, z_{\mathrm{pm}}^{(2)})}. \tag{50}$$

This expression contains all the information needed to design grating profiles with the desired gain and phase spectra. First, the total logarithmic gain is equal to the sum of the individual gains. Using the Rosenbluth factors, we obtain the total logarithmic gain in terms of the chirp rates:

$$\ln G(\delta\omega) = \frac{\pi\gamma^2(z_{\mathrm{pm}}^{(1)})}{|\kappa'(z_{\mathrm{pm}}^{(1)})|} + \frac{\pi\gamma^2(z_{\mathrm{pm}}^{(2)})}{|\kappa'(z_{pm}^{(2)})|}. \tag{51}$$

Second, the accumulated phase corresponds to the delay accumulated by the propagation at the idler velocity between the two PPMPs. Differentiating the total phase with respect to frequency, we can express the total group delay in terms of the positions of the PPMPs:

$$\tau(\delta\omega) = \frac{z_{\mathrm{pm}}^{(1)} - z_0^{(1)}}{v_s} + \frac{z_L^{(1)} - z_{\mathrm{pm}}^{(1)}}{v_i} + \frac{z_{\mathrm{pm}}^{(2)} - z_0^{(2)}}{v_i} + \frac{z_L^{(2)} - z_{\mathrm{pm}}^{(2)}}{v_s}. \tag{52}$$

The group delay for a particular spectral component corresponds to traveling from the input to the first PPMP at the signal group velocity, from the first to the second PPMPs at the idler group velocity, and then from the second PPMP to the end of the crystal at the signal group velocity. By choosing the lengths of the two crystals and the trajectory of the two PPMPs as a function of frequency, there are enough degrees of freedom to flatten the group delay over a broad spectrum [26].

5. OPTICAL PARAMETRIC AMPLIFICATION IN THE LOW-GAIN LIMIT

When the gain is low, we can assume that the signal wave remains unamplified and that only the idler grows. This process is called DFG. DFG and SHG in chirped QPM gratings have been studied in detail by Imeshev *et al.* [22,23]. They have shown that the spectrum of the generated wave is related to the spectrum of the input by a transfer function that is given by the Fourier transform of the grating profile. In the case of linearly chirped gratings, this transfer function can be expressed in terms of Fresnel integrals. Its spectrum is broad and flat with rapid oscillations, similar to the gain spectrum of chirped-grating OPAs.

We can recover these results by considering parametric amplification, Eqs. (3) and (4), in the low-gain limit. In this case, the signal amplitude is constant, and the evolution of the idler is described by a single first-order differential equation that can be integrated in a straightforward manner:

$$A_i(z) = i\gamma A_s^* \int_{z_0}^{z} e^{i\phi(z')} \mathrm{d}z'. \tag{53}$$

In the case of linearly chirped gratings, $\phi(z)$ is quadratic, and the solution can be expressed in terms of error functions or Fresnel integrals [22,23]. Alternatively, the integral can be approximately evaluated using the stationary phase method [31]:

$$A_i(z) \approx ie^{i\pi/4}\gamma\sqrt{\frac{2\pi}{\kappa'}} A_s^* e^{-(i/2)\kappa'(z_0 - z_{\mathrm{pm}})^2}. \tag{54}$$

The gain, which was given by the Rosenbluth gain factor in the case of parametric amplification, is now equal to $\gamma\sqrt{2\pi/\kappa'} \ll 1$. Nevertheless, both regimes are similar in two aspects: their gain is essentially constant over a wide bandwidth, and the idler wave experiences group-velocity dispersion through the frequency dependence of the PPMP. Although their mathematical descriptions differ, the physics of OPA and DFG are very similar.

6. CONCLUSION

In this paper, we presented a general procedure for the design of OPAs using nonuniform QPM gratings. The model used was 1D and assumed an undepleted, time-independent pump wave. We considered slow-varying but otherwise general profiles for the coupling coefficient and the wave vector mismatch. We treated the problem in the frequency domain.

We solved for the wave evolution using the complex WKB method. These expressions were then simplified to reveal the main features of the amplification process. We illustrated the use of the design formula by studying a variety of QPM grating profiles. We considered the canonical linear profile, which provides gain over wide bandwidths; tapered profiles for ripple reduction; sinusoidal profiles for selective frequency amplification; and finally, a tandem-grating design for engineered gain and group delay spectra (such as flat profiles for both).

We also discussed the similarities existing between parametric amplification in chirped QPM gratings and its low-gain limit DFG. The analysis presented here dealt exclusively with the spectral properties of the amplifiers. In a companion paper [28], we present the time-domain analysis, which will lead to a discussion of the temporal properties of the amplified pulses.

The 1D model presented here ignored transverse effects such as diffraction and noncollinear interactions. A 2D model including those effects will be described in future publications.

APPENDIX A: DERIVATION OF THE GENERAL WENTZEL–KRAMERS–BRILLOUIN SOLUTIONS

We consider profiles for which $\kappa(z)$ is a smooth, monotonic function of position. The smoothness condition is required for the validity of the WKB method. Monotonicity is also important because it ensures that there exists only one PPMP at any given input frequency. We can define a characteristic chirp rate, κ_0', which sets the scale of $\kappa(z)$. [In other words, we decompose the wavenumber mismatch into a linear part, $\kappa_0'(z-z_{\mathrm{pm}0})$, and another function that represents the departure from linearity.] We assume that this chirp rate is positive. The solution for the negative chirp rate can then be obtained using the substitutions $\kappa' \to -\kappa'$, $A_s \to A_s^*$, and $A_i \to -A_i^*$.

We normalize the position axis using the characteristic chirp rate κ_0':

$$\zeta = \sqrt{\kappa_0'}(z - z_{\mathrm{pm}}), \tag{A1}$$

where z_{pm} is the PPMP satisfying $\kappa(z_{\mathrm{pm}})=0$. Then Eq. (6) becomes

$$\frac{\mathrm{d}^2 a_s}{\mathrm{d}\zeta^2} + \bar{Q}(\zeta) a_s = 0, \tag{A2}$$

where

$$\bar{Q}(\zeta) = \left(\frac{\bar{\kappa}}{2} - \frac{i}{4}\frac{\lambda'}{\lambda}\right)^2 - \lambda + \frac{i\bar{\kappa}'}{2} + \frac{1}{4}\left(\frac{\lambda'}{\lambda}\right)'. \tag{A3}$$

In this expression, $\bar{\kappa} = \kappa/\kappa_0'^{1/2}$ is the normalized wavenumber mismatch, $\lambda = \gamma^2/\kappa_0'$ is the Rosenbluth gain exponent, and the primes denote differentiation with respect to ζ. Since the profiles κ and γ are, by assumption, smooth functions of position, we neglect small terms such as λ'' or $(\lambda')^2$ from now on. The solution is also subject to the boundary conditions:

$$a_s(\zeta_0) = \gamma^{-1/2}(\zeta_0) A_{s0}, \tag{A4}$$

$$\frac{\mathrm{d}a_s(\zeta_0)}{\mathrm{d}\zeta} = \gamma^{-1/2}(\zeta_0)\left[i\lambda^{1/2}(\zeta_0)A_{i0}^* - \frac{i}{2}\bar{\kappa}(\zeta_0)A_{s0} - \frac{1}{4}\frac{\lambda'(\zeta_0)}{\lambda(\zeta_0)}A_{s0}\right]. \tag{A5}$$

These come from the input conditions $A_s(z_0)=A_{s0}$, $A_i(z_0)=A_{i0}$, where z_0 is the position of the input plane in real units.

Equation (A2) is in a form suitable for WKB analysis. Its two linearly independent WKB solutions are [31–34]

$$\bar{Q}^{-1/4} \exp\left(\pm i \int^{\zeta} [\bar{Q}(\zeta')]^{1/2} \mathrm{d}\zeta'\right). \tag{A6}$$

The conditions of validity of the WKB approximation will be discussed below. As observed in Section 2 and illustrated in Fig. 2, the solutions are of an exponential type between the turning points, where $\mathrm{Re}(\bar{Q})<0$ (region II) and of an oscillatory type outside the interaction region where $\mathrm{Re}(\bar{Q})>0$ (regions I and III).

Approximations to the signal and idler waves can be written as linear combinations of these elementary WKB solutions. As we will see, different linear combinations are required in each of regions I–III. One way of calculating the correct coefficients is to use connection formulas to match the WKB solutions on either side of each turning point [31]. Another, possibly more elegant, approach is to employ the complex WKB method [32,34], which consists in extending the solution to the entire complex plane and enforcing continuity asymptotically far from the turning points. In this paper we will take the second approach. The procedure for doing so is detailed in Appendix B.

APPENDIX B: APPLICATION OF THE COMPLEX WENTZEL–KRAMERS–BRILLOUIN METHOD

In this section we apply the complex WKB method to extend each elementary solution to the entire complex plane. We establish the Stokes diagram corresponding to the function Q and the use of the usual rules for crossing Stokes and anti-Stokes lines. (Complete accounts of these procedures are given by Heading [32], Budden [34], and White [37].)

To uniquely define the WKB solutions we have to specify the lower bound of integration. It is typical to take one of the two complex turning points ζ_1 and ζ_2, which are the values of ζ for which $\bar{Q}=0$. Following Heading [32], we represent the WKB solutions by the notation

$$(\zeta_1, \zeta) \equiv \bar{Q}^{-1/4} \exp\left(i \int_{\zeta_1}^{\zeta} [\bar{Q}(\zeta')]^{1/2} \mathrm{d}\zeta'\right), \tag{B1}$$

$$(\zeta, \zeta_1) \equiv \bar{Q}^{-1/4} \exp\left(i \int_{\zeta}^{\zeta_1} [\bar{Q}(\zeta')]^{1/2} \mathrm{d}\zeta'\right). \tag{B2}$$

Moreover, and still following Heading, we will use the subscripts d or s according to whether a solution is asymptotically dominant (exponentially growing) or subdominant (exponentially decaying) as $|\zeta| \to \infty$.

The Stokes diagram of the function $\bar{Q}$ is shown in Fig. 11. We assume that the turning points are well separated. From each turning point emerges a branch cut, which we specify to be away from the real axis: three Stokes lines on which $\mathrm{Re}(\bar{Q}^{1/2}\mathrm{d}\zeta)=0$, where the magnitude of the two WKB solutions are most different; and three anti-Stokes lines on which $\mathrm{Im}(\bar{Q}^{1/2}\mathrm{d}\zeta)=0$, where the two solutions have equal magnitude. We number the various regions

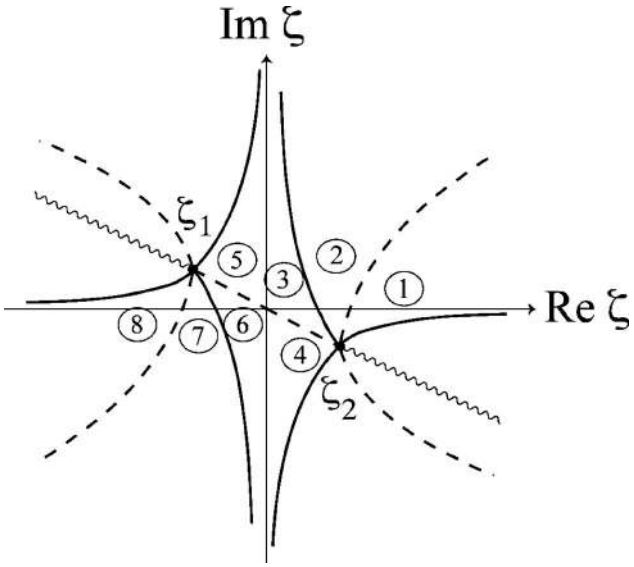

Fig. 11. Stokes diagram of the function $\bar{Q}$ defined by Eq. (A3). Solid curve, anti-Stokes curves; dashed curves, Stokes curves; zig–zag, branch cut.

from 1 through 8 as shown in Fig. 11. Our goal is to determine how each global WKB solution becomes a different linear combination of (ζ_1,ζ) and (ζ,ζ_1) or (ζ_2,ζ) and (ζ,ζ_2) when ζ moves from one region to another in the complex plane.

Let us start from (ζ_1,ζ) in region 8 ($\mathrm{Re}(\zeta)\to-\infty$). This solution being dominant in this sector, we write

$$\text{region 8:}\quad (\zeta_1,\zeta)_d. \tag{B3}$$

To go to region 7 we cross a Stokes line in the counterclockwise direction, so we must add the subdominant solution multiplied by the Stokes coefficient i:

$$\text{region 7:}\quad (\zeta_1,\zeta)_d + i(\zeta,\zeta_1)_s. \tag{B4}$$

To get to region 6, we cross an anti-Stokes line and the roles of dominance and subdominance are interchanged

$$\text{region 6:}\quad (\zeta_1,\zeta)_s + i(\zeta,\zeta_1)_d. \tag{B5}$$

Again, as we cross the Stokes line to go to region 5, we must add the subdominant solution:

$$\text{region 5:}\quad (\zeta_1,\zeta)_s + i\{(\zeta,\zeta_1)_d + i(\zeta_1,\zeta)_s\} = i(\zeta,\zeta_1)_d. \tag{B6}$$

We can match regions 5 and 3 by connecting turning points ζ_1 and ζ_2:

$$\text{region 3:}\quad i[\zeta_2,\zeta_1](\zeta,\zeta_2)_s, \tag{B7}$$

where we have introduced the coefficient

$$[\zeta_2,\zeta_1] \equiv \exp\left(i\int_{\zeta_2}^{\zeta_1}[Q(\zeta')]^{1/2}\mathrm{d}\zeta'\right). \tag{B8}$$

In region 2, this solution becomes dominant:

$$\text{region 2:}\quad i[\zeta_2,\zeta_1](\zeta,\zeta_2)_d. \tag{B9}$$

Finally, as we cross the Stokes line between regions 2 and 1 in the clockwise direction, we add the subdominant solution multiplied by $-i$:

$$\text{region 1:}\quad i[\zeta_2,\zeta_1]\{(\zeta,\zeta_2)_d - i(\zeta_2,\zeta)_s\}. \tag{B10}$$

Thus we obtain the continuation in the complex plane. In particular, we have a representation of the asymptotic behavior of this solution over the entire real axis.

Now let us consider the second solution. We start from (ζ,ζ_1) in region 8. Proceeding as before, we have the following connections:

$$\text{region 8:}\quad (\zeta,\zeta_1)_s, \tag{B11}$$

$$\text{region 7:}\quad (\zeta,\zeta_1)_s, \tag{B12}$$

$$\text{region 6:}\quad (\zeta,\zeta_1)_d, \tag{B13}$$

$$\text{region 5:}\quad (\zeta,\zeta_1)_d + i(\zeta_1,\zeta)_s, \tag{B14}$$

$$\text{region 3:}\quad [\zeta_2,\zeta_1](\zeta,\zeta_2)_s + i[\zeta_1,\zeta_2](\zeta_2,\zeta)_d \approx [\zeta_2,\zeta_1](\zeta,\zeta_2)_s, \tag{B15}$$

$$\text{region 2:}\quad [\zeta_2,\zeta_1](\zeta,\zeta_2)_d, \tag{B16}$$

$$\text{region 1:}\quad [\zeta_2,\zeta_1]\{(\zeta,\zeta_2)_d - i(\zeta_2,\zeta)_s\}. \tag{B17}$$

In going from regions 5 to 3, we have dropped the term with the coefficient $[\zeta_1,\zeta_2]$ because it is exponentially small compared to $[\zeta_2,\zeta_1]$. (This follows the assumption that the turning points are well separated.) We note that the two global solutions, which can be represented in region 8 by (ζ_1,ζ) and (ζ,ζ_1), only differ in region 1 by a factor of i.

APPENDIX C: WENTZEL–KRAMERS–BRILLOUIN SOLUTIONS FOR THE SIGNAL AND IDLER WAVES

In Appendix B we have given the proper asymptotic representations for two global, linearly independent solutions. Now we are left with the task of determining the linear combinations that satisfy the boundary conditions in Eqs. (A4) and (A5). Then each solution can be continued over the entire real axis using the results from Appendix B. We obtain the following solutions in each region:

$$a_s^{\mathrm{I}} \approx C_s^+(\zeta_1,\zeta) + C_s^-(\zeta,\zeta_1), \quad \zeta \ll -\zeta_{\mathrm{tp}}, \tag{C1}$$

$$a_s^{\mathrm{II}} \approx (iC_s^+ + C_s^-)(\zeta,\zeta_1), \quad -\zeta_{\mathrm{tp}} \ll \zeta \ll \zeta_{\mathrm{tp}}, \tag{C2}$$

$$a_s^{\mathrm{III}} \approx (iC_s^+ + C_s^-)[\zeta_2,\zeta_1](\zeta,\zeta_2)\left\{1 - i\frac{(\zeta_2,\zeta)}{(\zeta,\zeta_2)}\right\}, \quad \zeta \gg \zeta_{\mathrm{tp}}. \tag{C3}$$

The coefficients $C_s^{\pm}$ are given approximately (provided $\zeta_0 \ll -\zeta_{\mathrm{tp}}$) by

$$C_s^+ \approx \frac{1}{(\zeta_1,\zeta_0)\gamma^{1/2}(\zeta_0)}\left[\left(1 + \frac{\lambda(\zeta_0)}{\bar{\kappa}(\zeta_0)^2}\right)A_{s0} - \frac{\lambda^{1/2}(\zeta_0)}{\bar{\kappa}(\zeta_0)}A_{i0}^*\right], \tag{C4}$$

$$C_s^- \approx \frac{1}{(\zeta_0,\zeta_1)\gamma^{1/2}(\zeta_0)}\left(-\frac{\lambda(\zeta_0)}{\bar{\kappa}^2(\zeta_0)}A_{s0}+\frac{\lambda^{1/2}(\zeta_0)}{\bar{\kappa}(\zeta_0)}A_{i0}^*\right). \quad \text{(C5)}$$

The corresponding coefficients for the idler wave are obtained by interchanging the role of the signal and idler.

We recover the frequency-domain envelope functions by multiplying by $\gamma^{1/2}\exp(i\phi/2)$, resulting in the expression given in the text, Eq. (10). Even when only one wave is present initially (e.g., $A_{i0}=0$), the coefficients $C_s^{\pm}$ are in general both nonzero. The solution is then the superposition of a positive and a negative complex exponential, which interferes and causes the ripple observed on the amplification spectrum (as discussed in Subsection 4.C). These oscillations can be suppressed by letting either $\lambda(\zeta_0)\to 0$, $\lambda(\zeta_L)\to 0$ or $\bar{\kappa}(\zeta_0)\to\infty$, $\bar{\kappa}(\zeta_L)\to\infty$ (where ζ_L refers to the output plane). This is accomplished by the ripple-reduction techniques presented in Subsection 4.C.

APPENDIX D: VALIDITY OF THE WENTZEL–KRAMERS–BRILLOUIN SOLUTIONS

A few key assumptions have been made to obtain Eqs. (C1)–(C3). They will be examined in this section.

We have assumed when obtaining the continuation of the solution in the complex plane that the turning points are well separated. This requirement is necessary for the WKB solutions to be valid between the turning points. It also allowed us to drop the exponentially decaying solution when connecting between the turning points. In the case of a linear grating for which the magnitude of the amplification factor is $|[\zeta_2,\zeta_1]|=\exp(\pi\lambda)$, neglecting the decaying exponential is valid provided $\lambda\gg 1/\pi$. This value can be considered as the threshold of significant gain.

Second, we have assumed that neither turning point is close to the edges of the grating. This allowed us to define unambiguously the three regions I–III. The assumption that $\zeta_0\ll-\zeta_{\mathrm{tp}}$ was used to obtain the coefficients C^+ and C^-. Similarly, when obtaining expressions involving the position of the output of the grating, ζ_L, we assume that $\zeta_L\gg\zeta_{\mathrm{tp}}$. Consequently, the description given here ceases to be valid at the edges of the spectrum because our results cannot be applied if the gain region reaches the edges of the grating.

To summarize, the WKB formalism developed here is best suited when (i) the gain is large, (ii) the gain region is short compared to the grating length, and (iii) the PPMPs are far from the edges of the grating. In the case of the linear profile described in Subsection 4.B, these conditions are satisfied when $\lambda=\gamma^2/|\kappa'|\gg 1/\pi$, $L_g=4\gamma/|\kappa'|\ll L$, and $\delta\omega\ll\Delta\omega_{\mathrm{BW}}$.

APPENDIX E: EXPLICIT EXPRESSIONS FOR THE LINEAR PROFILE

Linear grating profiles are given simply by $\bar{\kappa}=\zeta$. Therefore, assuming a constant coupling coefficient, we have $\bar{Q}=\zeta^2/4-\lambda+i/2$. The complex turning points are then given by $\zeta_1,\zeta_2=\mp 2(\lambda-i/2)^{1/2}$.

In this case the integrals appearing in the WKB expressions can be evaluated exactly; approximate and simpler expressions are useful, however. First, for $\zeta_0\ll-\zeta_{\mathrm{tp}}$:

$$\int_a^{\zeta_0} Q^{1/2}\mathrm{d}\zeta' = (\lambda-i/2)\left\{\frac{\zeta_0}{2\sqrt{\lambda-i/2}}\sqrt{\frac{\zeta_0^2}{4(\lambda-i/2)}-1}+\ln\left[\frac{|\zeta_0|}{2\sqrt{\lambda-i/2}}+\sqrt{\frac{\zeta_0^2}{4(\lambda-i/2)}-1}\right]\right\}$$
$$\approx -\frac{\zeta_0^2}{4}+(\lambda-i/2)\ln\left(\frac{|\zeta_0|}{\lambda^{1/2}}\right)+\frac{\lambda}{2}. \quad \text{(E1)}$$

For $-\zeta_{\mathrm{tp}}\ll\zeta\ll\zeta_{\mathrm{tp}}$:

$$\int_a^{\zeta} Q^{1/2}\mathrm{d}\zeta' \approx i\sqrt{\lambda}\left(1-\frac{i}{4\lambda}\right)\zeta+\frac{i\pi\lambda}{2}+\frac{\pi}{4}. \quad \text{(E2)}$$

Similarly, for $\zeta_L\gg\zeta_{\mathrm{tp}}$:

$$\int_b^{\zeta_L} Q^{1/2}\mathrm{d}\zeta' \approx \frac{\zeta_L^2}{4}-(\lambda-i/2)\ln\left(\frac{\zeta_L}{\lambda^{1/2}}\right)-\frac{\lambda}{2}. \quad \text{(E3)}$$

Finally, the integral between the two turning points is simply

$$\int_a^b Q^{1/2}\mathrm{d}\zeta' = i\pi(\lambda-i/2). \quad \text{(E4)}$$

The solutions for the linear profile can then be written approximately as

$$A_s^{\mathrm{I}}(\zeta)\approx[(1+\epsilon^2(\zeta_0))A_{s0}+\epsilon(\zeta_0)A_{i0}^*]\exp\left(i\lambda\ln\left|\frac{\zeta}{\zeta_0}\right|\right)\times\left[1-\epsilon(\zeta)\left(\frac{A_{i0}^*+\epsilon(\zeta_0)A_{s0}}{A_{s0}+\epsilon(\zeta_0)A_{i0}^*}\right)\times\exp\left(\frac{i}{2}(\zeta^2-\zeta_0^2)-2i\lambda\ln\left|\frac{\zeta}{\zeta_0}\right|\right)\right], \quad \text{(E5)}$$

$$A_s^{\mathrm{II}}(\zeta)\approx\frac{1}{\sqrt{2}}\exp\left[\frac{\pi\lambda}{2}+\lambda^{1/2}\zeta-i\left(\frac{\zeta}{4\lambda^{1/2}}+\frac{\zeta^2}{4}+\lambda\ln\epsilon(\zeta_0)-\frac{\lambda}{2}\right)\right]\times[(1+\epsilon^2(\zeta_0))A_{s0}-\epsilon(\zeta_0)A_{i0}^*-(A_{i0}^*-\epsilon(\zeta_0)A_{s0})\times\exp(-i\Phi(\zeta_0))], \quad \text{(E6)}$$

$$A_s^{\mathrm{III}}(\zeta)\approx\exp\left(\pi\lambda+i\lambda\ln\left|\frac{\zeta}{\zeta_0}\right|\right)\times F(\zeta)[F^*(\zeta_0)A_{s0}-F(\zeta_0)e^{-i\Phi(\zeta_0)}A_{i0}^*], \quad \text{(E7)}$$

with

$$F(\zeta)=1-\epsilon(\zeta)\exp(i\Phi(\zeta)), \quad \text{(E8)}$$

$$\Phi(\zeta)=\frac{\zeta^2}{2}+2\lambda\ln\epsilon(\zeta)-\lambda+\frac{\pi}{2}, \quad \text{(E9)}$$

$$\epsilon(\zeta) = \frac{\lambda^{1/2}}{|\zeta|}. \tag{E10}$$

The expressions for the signal wave are obtained, as usual, by interchanging the signal and idler subscripts.

The spatial evolution of the signal and idler magnitudes for typical parameter values is plotted in Fig. 12 along with the numerical solution. The solutions are oscillatory before and after the gain region where the interaction is phase mismatched while they grow exponentially in the phase-matched region. As expected, the WKB solution is not a very good approximation in the vicinity of the turning points.

Finally, it is interesting to point out that the ripple-reduction schemes described in Subsection 4.C (namely, reduction of γ or increase of κ at the ends of the grating) amount to reducing the values of $\epsilon(\zeta_0)$ and $\epsilon(\zeta_L)$. Setting $\epsilon(\zeta_0)=\epsilon(\zeta_L)=0$ into Eqs. (E5)–(E7) leads to major simplifications:

$$A_s^{\mathrm{I}}(\zeta) \approx A_{s0} e^{i\lambda \ln|\zeta/\zeta_0|}, \tag{E11}$$

$$A_s^{\mathrm{II}}(\zeta) \approx \frac{1}{\sqrt{2}}[A_{s0} + iA_{i0}^* e^{-i(\zeta_0^2/2-\lambda)}] \times \exp\left[\frac{\pi\lambda}{2} + \lambda^{1/2}\zeta - i\left(\frac{\zeta}{4\lambda^{1/2}} + \frac{\zeta^2}{4} - \frac{\lambda}{2}\right)\right], \tag{E12}$$

$$A_s^{\mathrm{III}}(\zeta) \approx e^{\pi\lambda}[A_{s0} + iA_{i0}^* e^{-i(\zeta_0^2/2-\lambda)}] e^{i\lambda \ln|\zeta/\zeta_0|}. \tag{E13}$$

APPENDIX F: DERIVATION OF THE SIMPLIFIED DESIGN FORMULA

The WKB solutions, Eqs. (C1)–(C3), are quite complicated as they involve several integrals of the function $\bar{Q}^{1/2}$. To simplify these expressions, the integrals can be approximately evaluated for general (smooth) grating profiles.

Let us outline the evaluation procedure using as an example $\int_{\zeta_2}^{\zeta_L} \bar{Q}^{1/2} \mathrm{d}\zeta$. We neglect the variation of the coupling coefficient, therefore we can approximate $\bar{Q}$ from Eq. (A3) as $\bar{Q} \approx \bar{\kappa}^2/4 - \lambda + i\bar{\kappa}'/2$. The integral can be separated into two parts. The first one corresponds to the vicinity of the turning point, where $\bar{\kappa}(z)$ is approximately linear; the second one corresponds to the portion away from the turning point, where $\bar{\kappa}$ is large. Thus the two integration ranges are from ζ_2 to $\tilde{\zeta}$, and from $\tilde{\zeta}$ to ζ_L, respectively, with $\tilde{\zeta}$ located on the real axis somewhere between $\mathrm{Re}(\zeta_2)$ and ζ_L, close enough to ζ_2 so that $\bar{\kappa}$ is linear but far enough so that the behavior of $\bar{Q}$ is dominated by $\bar{\kappa}^2/4$. The integral over the linear range is given by Eq. (E3). Retaining the most significant real and imaginary contributions, we have

$$\int_{\zeta_2}^{\tilde{\zeta}} \bar{Q}^{1/2} \mathrm{d}\zeta \approx \frac{\bar{\kappa}^2}{4} + \frac{i}{2} \ln\left(\frac{\tilde{\zeta}}{\lambda^{1/2}}\right). \tag{F1}$$

The second integral can be approximated by

$$\int_{\tilde{\zeta}}^{\zeta_L} \bar{Q}^{1/2} \mathrm{d}\zeta \approx \frac{1}{2}\int_{\tilde{\zeta}}^{\zeta_L} \bar{\kappa} \mathrm{d}\zeta + \frac{i}{2} \ln\left(\frac{\bar{\kappa}(\zeta_L)}{\tilde{\zeta}}\right). \tag{F2}$$

Adding both contributions gives

$$\int_{\zeta_2}^{\zeta_L} \bar{Q}^{1/2} \mathrm{d}\zeta \approx \frac{1}{2}\int_{0}^{\zeta_L} \bar{\kappa} \mathrm{d}\zeta + \frac{i}{2} \ln\left(\frac{\bar{\kappa}(\zeta_L)}{\lambda^{1/2}}\right). \tag{F3}$$

The integral $\int_{\zeta_1}^{\zeta_0} \bar{Q}^{1/2} \mathrm{d}\zeta$ can be evaluated in a similar manner. Using these approximations, the elementary WKB solutions can be written as

$$(\zeta_1, \zeta_0) \approx 2^{1/2} \lambda^{-1/4}(\zeta_0) e^{i/2\int_{\zeta_0}^{0} \kappa(\zeta)\mathrm{d}\zeta}, \tag{F4}$$

$$(\zeta_0, \zeta_1) \approx \frac{2^{1/2}\lambda^{1/4}(\zeta_0)}{|\kappa(\zeta_0)|} e^{-i/2\int_{\zeta_0}^{0} \kappa(\zeta)\mathrm{d}\zeta}, \tag{F5}$$

$$(\zeta_2, \zeta_L) \approx \frac{2^{1/2}\lambda^{1/4}(\zeta_0)}{\kappa(\zeta_L)} e^{i/2\int_{0}^{\zeta_L} \kappa(\zeta)\mathrm{d}\zeta}, \tag{F6}$$

$$(\zeta_L, \zeta_2) \approx 2^{1/2} \lambda^{-1/4}(\zeta_0) e^{-i/2\int_{0}^{\zeta_L} \kappa(\zeta)\mathrm{d}\zeta}. \tag{F7}$$

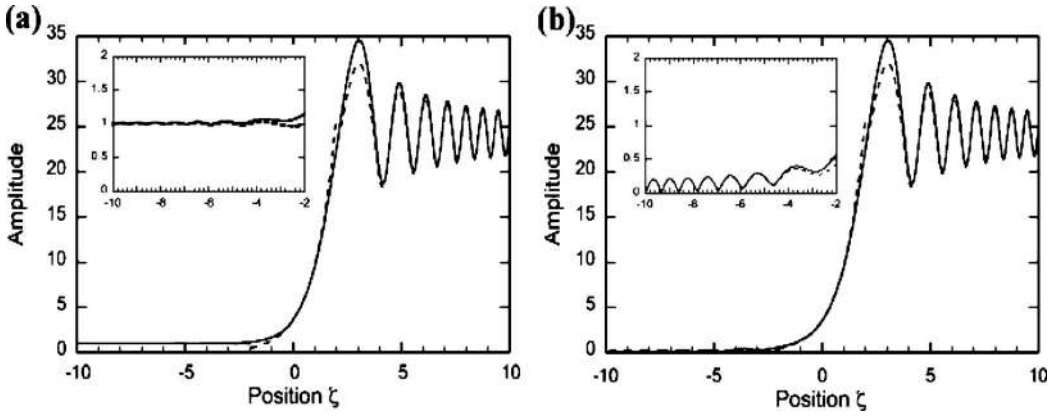

Fig. 12. Comparison between the WKB solution and the numerical solution for $\lambda=1$, $A_{s0}=1$, $A_{i0}=0$, $\bar{L}=20$, and ζ_{pm} located at the center of the grating: (a) signal, (b) idler. The insets give details on the amplitudes near the input.

Similarly, the amplification factor can be approximated by

$$[\zeta_2,\zeta_1]=e^{i\int_{\zeta_2}^{\zeta_1}\bar{Q}^{1/2}\mathrm{d}\zeta}\approx -ie^{\int_{\zeta_1^*}^{\zeta_2^*}(\lambda-\bar{\kappa}^2/4)^{1/2}\mathrm{d}\zeta}, \tag{F8}$$

where $\zeta_{1,2}^*$ are the real-valued turning points of $\lambda-\bar{\kappa}^2(\zeta)/4$. These approximations can then be substituted into the expressions for the signal and idler, Eq. (C3), to yield the following formula valid for general smooth grating profiles:

$$\begin{aligned}A_s^{\mathrm{III}}\approx&\left[\left(1-\frac{i\lambda^{1/2}(\zeta_0)}{\kappa(\zeta_0)}e^{i\int_{\zeta_0}^0\kappa(\zeta)\mathrm{d}\zeta}\right)A_{s0}+ie^{i\int_{\zeta_0}^0\kappa(\zeta)\mathrm{d}\zeta}\right.\\&\left.\times\left(1+\frac{i\lambda^{1/2}(\zeta_0)}{\kappa(\zeta_0)}e^{-i\int_{\zeta_0}^0\kappa(\zeta)\mathrm{d}\zeta}\right)A_{i0}^*\right]\\&\times e^{\int_{\zeta_1^*}^{\zeta_2^*}(\lambda-\bar{\kappa}^2/4)^{1/2}\mathrm{d}\zeta}\left(1-\frac{i\lambda^{1/2}(\zeta_L)}{\kappa(\zeta_L)}e^{i\int_0^{\zeta_L}\kappa(\zeta)\mathrm{d}\zeta}\right).\end{aligned} \tag{F9}$$

To simplify the formulas further, we neglect the oscillatory terms. This step yields

$$A_s\approx[A_{s0}+iA_{i0}^*e^{i\int_{\zeta_0}^0\bar{\kappa}\mathrm{d}\zeta}]e^{\int_{\zeta_1^*}^{\zeta_2^*}(\lambda-\bar{\kappa}^2/4)^{1/2}\mathrm{d}\zeta}, \tag{F10}$$

which is the design formula, Eq. (14).

ACKNOWLEDGMENTS

This work was sponsored by the Air Force Office of Scientific Research (AFOSR) under AFOSR grants F49620-02-1-0240 and F49620-01-1-0428. M. Charbonneau-Lefort acknowledges additional support from the Natural Sciences and Engineering Research Council of Canada. The work of B. Afeyan was supported by the Laser-Plasma branch of the Naval Research Laboratory and by a Department of Energy (DOE) National Nuclear Security Administration (NNSA) Stewardship Science Academic Alliances (SSAA) grant.

REFERENCES

1. S. Backus, C. G. Durfee, M. M. Murnane, and H. C. Kapteyn, "High power ultrafast lasers," Rev. Sci. Instrum. **69**, 1207–1223 (1998).
2. C. G. Durfee, S. Backus, M. M. Murnane, and H. C. Kapteyn, "Design and implementation of a TW-class high-average power laser system," IEEE J. Sel. Top. Quantum Electron. **4**, 395–406 (1988).
3. P. Maine, D. Strickland, P. Bado, M. Pessot, and G. Mourou, "Generation of ultrahigh peak power pulses by chirped pulse amplification," IEEE J. Quantum Electron. **24**, 398–403 (1988).
4. W. Joosen, P. Agostini, G. Petite, J. P. Chambaret, and A. Antonetti, "Broadband femtosecond infrared parametric amplification in β-BaB_2O_4," Opt. Lett. **17**, 133–135 (1992).
5. G. M. Gale, M. Cavallari, T. J. Driscoll, and F. Hache, "Sub-20-fs tunable pulses in the visible from an 82-MHz optical parametric oscillator," Opt. Lett. **20**, 1562–1564 (1995).
6. G. M. Gale, F. Hache, and M. Cavallari, "Broad-bandwidth parametric amplification in the visible: femtosecond experiments and simulations," IEEE J. Sel. Top. Quantum Electron. **4**, 224–229 (1998).
7. A. Dubietis, G. Jonuŝauskas, and A. Piskarskas, "Powerful femtosecond pulse generation by chirped and stretched pulse parametric amplification in BBO crystal," Opt. Commun. **88**, 437–440 (1992).
8. I. Jovanovic, C. Ebbers, and C. P. J. Barty, "Hybrid chirped-pulse amplification," Opt. Lett. **27**, 1622–1624 (2002).
9. I. Jovanovic, B. J. Comaskey, C. A. Ebbers, R. A. Bonner, D. M. Pennington, and E. C. Morse, "Optical parametric chirped-pulse amplifier as an alternative to Ti:sapphire regenerative amplifiers," Appl. Opt. **41**, 2923–2929 (2002).
10. I. Jovanovic, C. G. Brown, C. A. Ebbers, C. P. J. Barty, N. Forget, and C. L. Blanc, "Generation of high-contrast millijoule pulses by optical parametric chirped-pulse amplification in periodically poled $KTiOPO_4$," Opt. Lett. **30**, 1036–1038 (2005).
11. A. Shirakawa and T. Kobayashi, "Noncollinearly phase-matched femtosecond optical parametric amplification with a 2000 cm^{-1} bandwidth," Appl. Phys. Lett. **72**, 147–149 (1998).
12. A. Shirakawa, I. Sakane, M. Takasaka, and T. Kobayashi, "Sub-5-fs visible pulse generation by pulse-front-matched noncollinear optical parametric amplification," Appl. Phys. Lett. **74**, 2268–2270 (1999).
13. T. Kobayashi and A. Baltuska, "Sub-5 fs pulse generation from a noncollinear optical parametric amplifier," Meas. Sci. Technol. **13**, 1671–1682 (2002).
14. M. M. Fejer, G. A. Magel, D. H. Jundt, and R. L. Byer, "Quasi-phase-matched second harmonic generation: tuning and tolerances," IEEE J. Quantum Electron. **28**, 2631–2654 (1992).
15. A. Galvanauskas, M. A. Arbore, M. M. Fejer, M. E. Fermann, and D. Harter, "Fiber-laser-based femtosecond parametric generator in bulk periodically poled $LiNbO_3$," Opt. Lett. **22**, 105–107 (1997).
16. A. Galvanauskas, A. Hariharan, D. Harter, M. A. Arbore, and M. M. Fejer, "High-energy femtosecond pulse amplification in a quasi-phase-matched parametric amplifier," Opt. Lett. **23**, 210–212 (1998).
17. A. Galvanauskas, D. Harter, M. A. Arbore, M. H. Chou, and M. M. Fejer, "Chirped-pulse-amplification circuits for fiber amplifiers, based on chirped-period quasi-phase-matching gratings," Opt. Lett. **23**, 1695–1697 (1998).
18. T. Suhara and H. Nishihara, "Theoretical analysis of waveguide second-harmonic generation phase matched with uniform and chirped gratings," IEEE J. Quantum Electron. **26**, 1265–1276 (1990).
19. M. A. Arbore, A. Galvanauskas, D. Harter, M. H. Chou, and M. M. Fejer, "Engineerable compression of ultrashort pulses by use of second-harmonic generation in chirped-period-poled lithium niobate," Opt. Lett. **22**, 1341–1343 (1997).
20. M. A. Arbore, O. Marco, and M. M. Fejer, "Pulse compression during second-harmonic generation in aperiodic quasi-phase-matching gratings," Opt. Lett. **22**, 865-867 (1997).
21. G. Imeshev, A. Galvanauskas, D. Harter, M. A. Arbore, M. Proctor, and M. M. Fejer, "Engineerable femtosecond pulse shaping by second-harmonic generation with Fourier synthetic quasi-phase-matching gratings," Opt. Lett. **23**, 864–866 (1998).
22. G. Imeshev, M. A. Arbore, M. M. Fejer, A. Galvanauskas, M. Fermann, and D. Harter, "Ultrashort-pulse second-harmonic generation with longitudinally nonuniform quasi-phase-matching gratings: pulse compression and shaping," J. Opt. Soc. Am. B **17**, 304–318 (2000).
23. G. Imeshev, M. M. Fejer, A. Galvanauskas, and D. Harter, "Pulse shaping by difference-frequency mixing with quasi-phase-matching gratings," J. Opt. Soc. Am. B **18**, 534–539 (2001).
24. K. L. Baker, "Single-pass gain in a chirped quasi-phase-matched optical parametric oscillator," Appl. Phys. Lett. **82**, 3841–3843 (2003).
25. T. Beddard, M. Ebrahimzadeh, T. D. Reid, and W. Sibbett, "Five-optical-cycle pulse generation in the mid infrared from an optical parametric oscillator based on aperiodically poled lithium niobate," Opt. Lett. **25**, 1052–1054 (2000).
26. M. Charbonneau-Lefort, M. M. Fejer, and B. Afeyan,

"Tandem chirped quasi-phase-matching grating optical parametric amplifier design for simultaneous group delay and gain control," Opt. Lett. **30**, 634–636 (2005).
27. M. N. Rosenbluth, "Parametric instabilities in inhomogeneous media," Phys. Rev. Lett. **29**, 565–567 (1972).
28. M. Charbonneau-Lefort, B. Afeyan, and M. M. Fejer, "Optical parametric amplifiers using chirped quasi-phase-matching gratings II: space-time evolution of light pulses," J. Opt. Soc. Am. B **25** (2008), to be published.
29. R. L. Byer, "Parametric oscillators and nonlinear materials," in *Nonlinear Optics*, P. G. Harper and B. S. Wherrett, eds. (Academic, 1977).
30. Y. R. Shen, *The Principles of Nonlinear Optics* (Wiley, 1984).
31. C. M. Bender and S. A. Orszag, *Advanced Mathematical Methods for Scientists and Engineers* (Springer-Verlag, 1999).
32. J. Heading, *An Introduction to Phase-Integral Methods* (Wiley, 1962).
33. M. V. Berry and K. E. Mount, "Semiclassical approximations in wave mechanics," Rep. Prog. Phys. **35**, 315–397 (1972).
34. K. G. Budden, *The Propagation of Radio Waves* (Cambridge U. Press, 1988).
35. G. Cirmi, D. Brida, C. Manzoni, M. Marangoni, S. De Silvestri, and G. Cerullo, "Few-optical-cycle pulses in the near-infrared from a noncollinear optical parametric amplifier," Opt. Lett. **32**, 2396–2398 (2007).
36. J. Huang, X. P. Xie, C. Langrock, R. V. Roussev, D. S. Hum, and M. M. Fejer, "Amplitude modulation and apodization of quasi-phase-matched interactions," Opt. Lett. **31**, 604–606 (2006).
37. R. B. White, *Asymptotic Analysis of Differential Equations* (Imperial College Press, 2005).